

2D THz Optoelectronics

Martin Mittendorff, Stephan Winnerl, and Thomas E. Murphy*

The terahertz (THz) region of the electromagnetic spectrum spans the gap between optics and electronics and has historically suffered from a paucity of optoelectronic devices, in large part because of inadequate optical materials that function in this spectral range. 2D materials, including graphene and a growing family of related van der Waals materials, have been shown to exhibit unusual optical and electrical properties that can enable diverse new applications in the THz regime. In this review, some of the unusual properties of 2D materials that make them promising for THz applications are explained, the recent work in the field of 2D THz optoelectronics is summarized, and the challenges and opportunities that await this promising new field are outlined.

1. Introduction

The terahertz (THz) region of the electromagnetic spectrum is loosely defined as ranging from 300 GHz (1 mm) to 30 THz (10 μm). THz waves penetrate most dry, nonconductive materials, but unlike X-rays they are nonionizing—making them an appealing alternative for nondestructive evaluation and security screening.^[1] Many large complex biological molecules exhibit characteristic vibrational resonances in the THz regime, and for this reason THz molecular spectroscopy has applications that include pharmaceutical manufacturing,^[2] chemical hazard detection,^[3] and even future planetary exploration missions to assess the origins of life in our solar system.^[4] THz (and sub-millimeter) waves could provide new means for point-to-point wireless communication at speeds that far surpass today's cellular and WiFi networks.^[5]

Many optoelectronic technologies that are commonplace in the optical or infrared regime, including lasers, detectors, and modulators, cannot be easily translated to this long-wavelength regime, because of limitations of the constituent materials. Traditional electronic materials are often too slow to permit switching, modulation, or actuation at THz

frequencies. With few exceptions, most optical glasses and dielectrics, though transparent in the visible regime, absorb strongly at THz frequencies. Semiconductor materials—a mainstay of traditional photonic devices—have a bandgap that far exceeds the THz photon energy, making them unsuitable for active THz optoelectronic devices like lasers and detectors.

2D materials have experienced a renaissance in the past decade, which began in 2004 with the experimental isolation and subsequent investigation of graphene. While graphene, a semimetal, remains the most widely explored and developed 2D

material, the range of atomically thin materials available today has greatly expanded to include insulators, semiconductors, and an endless variety of complex heterostructures formed by combining or stacking these materials. These 2D van der Waals materials can exhibit optical, electrical, mechanical, and thermal properties that are distinctly different from bulk materials or even thin films and can enable a variety of new optoelectronic devices.

In this review, we discuss the growing field of THz 2D optoelectronics, with an emphasis on the novel material properties and device applications that they enable. We begin here with a short introduction to the optical and electronic properties of 2D materials. In Section 2, we review several proposed and demonstrated methods for THz detectors that rely on 2D materials. Section 3 discusses THz modulators based on 2D materials, and Section 4 describes schemes for producing or emitting THz radiation. We conclude with a brief discussion of the challenges ahead and outlook for the field of 2D THz optoelectronics.

The development of 2D devices has been accompanied and aided by significant advances in the science of material development and manufacturing. In addition to mechanical (adhesive) exfoliation of 2D flakes from bulk, there now exist a variety of wafer-scale 2D manufacturing technologies including epitaxy, chemical vapor deposition, and liquid phase epitaxy. The subsequent processing of 2D materials has also evolved rapidly, to include a variety of film transfer processes, assembly and stacking processes that could in the future enable wafer-scale fabrication of 2D devices. This review does not seek to cover the advances in material fabrication or processing, and instead we refer the readers to other recent reviews and papers on the subject.^[6]

The unique properties of 2D materials that are most interesting and attractive for THz applications include i) the potential for high carrier mobility, ii) the capability of electrostatic gating, which allows for tuning of the optical and electrical properties, iii) unusual hot-carrier dynamics, iv) the possibility of heterogeneous integration, v) unconventional band structure, and vi) a sub-wavelength plasmonic response at THz frequencies—each of which we briefly discuss below.

Prof. M. Mittendorff
Fakultät für Physik – Experimentalphysik
Universität Duisburg-Essen
Lotharstr. 1, Duisburg 47057, Germany

Dr. S. Winnerl
Institute of Ion Beam Physics and Materials Research
Helmholtz-Zentrum Dresden-Rossendorf
Bautzner Landstraße 400, Dresden 01328, Germany

Prof. T. E. Murphy
Institute for Research in Electronics and Applied Physics
University of Maryland
College Park, MD 20740, USA
E-mail: tem@umd.edu

 The ORCID identification number(s) for the author(s) of this article can be found under <https://doi.org/10.1002/adom.202001500>.

DOI: 10.1002/adom.202001500

1.1. Carrier Mobility

The carrier mobility of a material, μ_C , quantifies the proportionality between an applied electric field and the resulting drift velocity of charged carriers (electrons or holes)

$$v_d = \mu_C E \quad (1)$$

The mobility, along with the carrier concentration determines the impedance of the material, and also controls the speed at which a material or transistor can be actuated or switched. Traditional semiconductors like silicon exhibits an electron mobility of $1400 \text{ cm}^2 \text{ V}^{-1} \text{ s}^{-1}$, and in GaAs the mobility can approach $10\,000 \text{ cm}^2 \text{ V}^{-1} \text{ s}^{-1}$ at room temperature. Graphene has been observed to have a room temperature mobility as high as $70\,000 \text{ cm}^2 \text{ V}^{-1} \text{ s}^{-1}$,^[7] and a low-temperature mobility up to $200\,000 \text{ cm}^2 \text{ V}^{-1} \text{ s}^{-1}$.^[8] Among the other 2D semiconducting materials, black phosphorus stands out for its mobility as high as $10\,000 \text{ cm}^2 \text{ V}^{-1} \text{ s}^{-1}$ ^[9] in bulk crystals and $1000 \text{ cm}^2 \text{ V}^{-1} \text{ s}^{-1}$ in atomically thin layers.^[10]

In 2D and bulk materials alike, the mobility depends strongly on the level of impurities, inhomogeneities, and imperfections in the material, and hence mobility is often used as a proxy for material quality and purity. In 2D materials, the mobility also depends strongly on the quality and flatness of the underlying substrate. Even amorphous dielectric films like thermal oxides are known to exhibit an atomic-level surface roughness that can limit the carrier mobility of the overlying 2D material.^[11] The highest observed mobility for 2D materials have been measured on freely-suspended membranes or in 2D sandwich structures that employ atomically smooth hexagonal boron nitride substrate and superstrates.

Not all 2D materials exhibit a high mobility, and not all THz applications require a high mobility. Nonetheless, carrier mobility remains one of the most commonly cited and readily measured 2D material properties, and it is fundamentally related to the THz conductivity of the material.

1.2. Electrostatic Gating and Tunability

In traditional semiconductors, the concentration and polarity of free carriers is determined by the species and concentration

of impurity dopants—donors or acceptor atoms from the neighboring columns of the periodic table that permanently contribute to the population of mobile electrons and holes. In metals, the carrier concentration depends primarily on the atomic density. While 2D materials can also be extrinsically or chemically doped in the same manner, because of their thin conductive nature, the carrier concentration can also be electrically controlled and actuated through the field effect. When an electrical contact is placed in proximity to a 2D material as shown in **Figure 1a**, separated by an insulating dielectric, they form a capacitive structure in which the areal charge density is approximately proportional to the normal electric field. In this way, a voltage applied between the electrical gate contact and the 2D material can be used to modulate the Fermi level in the material, thereby depleting or supplying free carriers, in much the same way that a field-effect transistor operates. In the THz regime, 2D materials can therefore be considered electrically tunable Drude conductors. It must be pointed out, however, that the need for a conductive gate contact poses a significant challenge for THz applications, because good conductors either screen or reflect the incident THz radiation, thereby inhibiting the interaction with the 2D material. The voltage required to modulate the carrier concentration increases linearly with the thickness of the intervening dielectric, and in most cases the gap must be held much smaller than $1 \mu\text{m}$ in order to allow efficient modulation with reasonable applied voltage. Because this thickness is much smaller than the terahertz wavelength, the gate electrode cannot be ignored when considering the THz response: the free charge carriers in the electrode material lead to a screening of the THz field, even when the gate is not facing the THz wave.

Electrically gated 2D THz structures have overcome this limitation by using ultrathin metallic layers,^[12] or weakly-doped semiconducting substrates,^[13] which offer sufficient electrical conductivity for gating at the expense of a modest amount of THz absorption. Another approach is to employ a second 2D material as a gate, such as graphene in place of a conventional conductor.

If the gate contact is lithographically patterned, it is possible to produce a spatially varying carrier concentration within the 2D material, and by employing adjacent gates, one can produce lateral p-n junctions within a 2D material. As discussed later, such structures have been used and proposed for THz detectors and emitters.

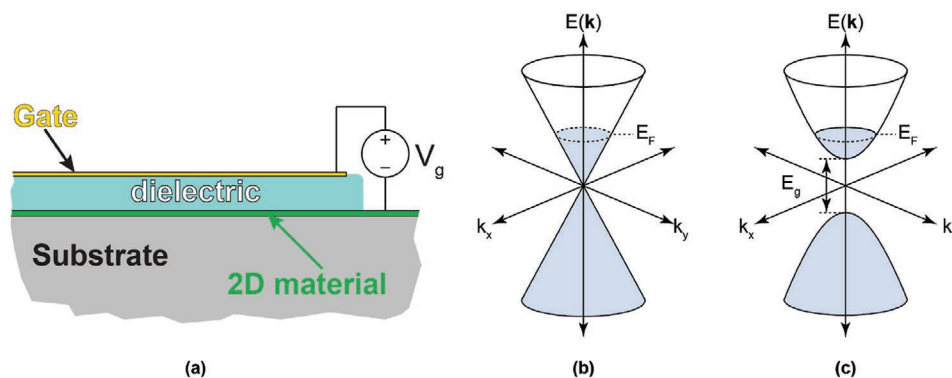


Figure 1. a) An adjacent electrical contact, separated from the 2D material by an insulating dielectric layer, can be used to electrostatically tune the carrier concentration in the 2D material. b) The electronic band-structure for graphene is composed of two symmetrical cones that touch at $k = 0$. The Fermi level can be electrostatically adjusted, thereby controlling the conductivity of the layer. c) Semiconducting 2D materials exhibit a bandgap, typically well above the THz regime, and can be gated to an insulating state.

1.3. Hot Carrier Dynamics

In most 2D materials, the absorption of THz radiation occurs primarily through intraband processes, in which the preexisting population of mobile carriers is excited and accelerated by an incident terahertz wave. Once excited, the carriers rapidly equilibrate among themselves through electron–electron interactions, achieving a transient carrier temperature that exceeds that of the atomic lattice. Eventually, the carriers relax to the lattice temperature, typically through impurity scattering and electron–phonon scattering. 2D materials exhibit unique thermal properties that make these hot-carrier processes strong and prominent. Graphene, for example, has a very small electronic heat capacity and anomalously weak electron–phonon scattering, and as a result hot carrier effects are significant and readily observed in graphene, even at room temperature. Hot carrier effects in graphene and black phosphorus have been exploited to realize fast, sensitive room temperature terahertz detectors based on the photothermoelectric and bolometric effects.^[14] The mechanisms of carrier cooling and relaxation in 2D materials depend sensitively on defects and impurities, and the dynamics of carrier excitation and relaxation are of paramount importance for a variety of THz device applications.

1.4. Heterogeneous Integration

One of the advantages of 2D materials is the possibility for heterogeneous integration with traditional materials and devices. The importance of this feature cannot be overstated, especially in the THz regime, where suitable low-loss optical materials are scarce. Most solid state materials, including dielectrics and semiconductors exhibit significant absorption in the THz regime, caused by free-carrier absorption or pervasive phonon absorption bands throughout this spectral regime. The absorption caused by these effects seldom contributes to (and more often impairs) the optoelectronic functionality of a device. Hence, THz optoelectronic devices often rely on a highly restricted set of low loss materials, such as intrinsic semiconductors, sapphire, crystalline quartz, and polymers like polytetrafluoroethylene.

2D materials can be readily incorporated into a variety of other structures, either by direct growth or by thin-film transfer methods, thereby greatly expanding the functionality of otherwise passive infrared materials.

1.5. Unconventional Band Structure

The range of 2D materials has expanded to include insulators direct- and indirect-bandgap semiconductors, as well as conductors. However, the prototypical and most widely studied and exploited 2D material is graphene—the 2D hexagonal lattice of carbon atoms. Graphene is a semimetal, with a linear band-structure at low energy that is expressed as

$$E(\mathbf{k}) = \pm \hbar v_F |\mathbf{k}| \quad (2)$$

where \mathbf{k} represents the in-plane 2D momentum vector relative to the K point, the proportionality constant v_F has units of

velocity, and is called the Fermi velocity, and the \pm symbol indicates the conduction or valence band, respectively. This is often termed a “relativistic” dispersion relation, because the form of (2) describes particles that obey the relativistic Dirac equation rather than the more traditional Schrodinger equation. Figure 1b depicts the band-structure of graphene in the vicinity of the K and K' points, which describes symmetrical Dirac cones that touch at zero energy. The occupancy of the energy levels is determined by the chemical potential (or in the limit of low temperature, the Fermi energy), which can be electrostatically adjusted, as discussed earlier to determine the overall carrier concentration.

The Dirac band structure has unique features that make it especially appealing for optoelectronic applications in the THz regime. Because graphene has no bandgap, it can absorb and interact with photons at all frequencies, including low-energy THz photons. In fact, because of the linear dispersion, graphene is both predicted and observed to exhibit a universal interband absorption of $\pi\alpha$ ($= 2.3\%$), where α represents the fine-structure constant.^[15] The symmetry in the band structure implies that electrons and holes behave identically, and hence the optical properties and carrier dynamics of p-type and n-type graphene are the same.

The optical properties of graphene, especially in the terahertz regime, can be described by two processes: intraband absorption in which free carriers from the conduction (or valence) band are excited or heated by incoming radiation, and interband absorption, in which electrons in the valence band are promoted to the conduction band through absorption of photons. Intraband absorption (also known as Drude absorption or free-carrier absorption) only occurs when there is a population of free carriers, as, for example, when the graphene is electrostatically doped. Interband absorption only occurs if there are both occupied states in the valence band and unoccupied vacant states in the conduction band with the same momentum \mathbf{k} . If the destination conduction band states are filled, because of electrostatic doping the promotion of electrons from the valence band is forbidden by the Pauli exclusion principle. In graphene, Pauli blocking occurs for frequencies

$$\hbar\omega < 2|E_F| \quad (3)$$

where E_F is the Fermi energy, and for this range of frequencies, intraband (Drude) absorption is the dominant optical process.

The electrostatic doping is not unique to graphene, and can also be applied in semiconducting 2D materials. Figure 1c depicts the band structure of an atomically thin 2D semiconductor with a direct bandgap denoted E_g . Semiconducting 2D materials include the family of transition metal dichalcogenides (TMDCs) such as MoS₂ and WSe₂, as well as black phosphorus. In most 2D semiconductors, the bandgap falls well above the THz range, which prohibits direct interband transitions. However, unlike Dirac materials, a semiconductor can be electrostatically doped to a near-insulating condition, making it transparent at THz frequencies. With the exception of black phosphorus, to date there are very few 2D semiconductors that exhibit a carrier mobility that rivals that attainable in graphene, which is another reason why graphene remains the most widely exploited 2D material for THz applications.

A greater variety of electronic band structures can be accessed and engineered by combining or stacking 2D heterostructures,^[16] with possible applications in light emission and population inversion.

1.6. Plasmonic Response

A surface plasmon is a collective charge density wave that propagates at the boundary of a conductive material. In traditional 3D metals like silver and gold, surface plasmons are confined to the skin depth of the material, and can have a wavelength that is smaller than the vacuum wavelength. The plasma frequency, ω_p , in typical 3D metals depends on the density of free carriers, and typically falls in the ultraviolet regime. As a consequence, propagating surface plasmons are typically observed only at visible or near-infrared wavelengths. In the lower-frequency THz and microwave regime, most metals behave as near-ideal conductors, and surface plasmon effects are therefore not prevalent.

2D conductors, by contrast, exhibit a distinctly different plasmonic behavior, primarily because the charge carriers are confined to a 2D sheet rather than to a volume defined by the skin depth.^[17] **Figure 2** compares the dispersion relation for a surface plasmon polariton wave at the surface of a 3D conductor (red) to that of a surface plasmon wave in a 2D conductive sheet (green). For 3D plasmons, the dispersion relation approaches the light line at frequencies far below the plasma frequency. For 2D plasmons, the dispersion relation can be approximated by^[18]

$$\omega(q) = \sqrt{\frac{e^2 E_F}{2\epsilon\pi\hbar}} q \quad (4)$$

Where E_F denotes the Fermi energy in the 2D material and ϵ is the dielectric permittivity of the surrounding medium. Because of this distinctive square-root dependence, the dispersion relation for 2D materials deviates significantly from the light-line even at THz frequencies, as depicted in **Figure 2**. Moreover, in 2D materials, the Fermi energy can be directly controlled via electrostatic gating, which means that the THz

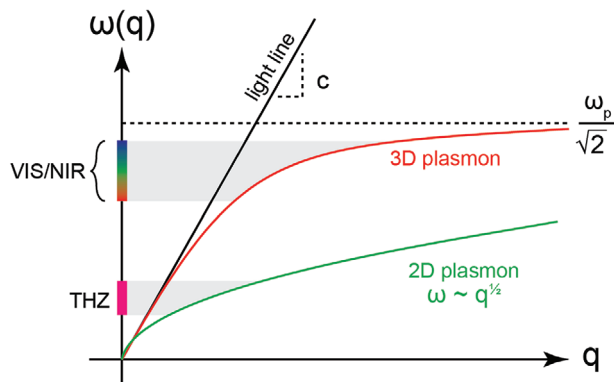


Figure 2. Illustration of dispersion relation (frequency ω vs wavevector q) for a plane wave in vacuum (black), a surface plasmon-polariton confined to the boundary of a 3D conductor (red), and a surface plasmon wave confined to a 2D conductive sheet (green).

response can be electrically tuned. The spatial wavelength of plasmons in 2D materials can be orders of magnitude smaller than the vacuum wavelength.

When the conductive sheet is patterned into micrometer-scale elements such as discs or ribbons, the plasmons are confined in standing wave modes that exhibit a distinct THz resonance frequency that depends on the geometry and Fermi energy.^[19] As explained in Sections 2–4, tunable 2D plasmonic resonances have been suggested for use in terahertz filters, modulators, detectors, and emitters.

2. THz Detection

2.1. General

The technology for THz detection has evolved over decades, and now includes a variety of different mechanisms and operating conditions. Present-day THz detection methods include Golyay cells, cryogenically-cooled bolometers based on Si or Ge, cryogenically-cooled extrinsic photoconductors (most commonly Ge:Ga), rectifiers like Schottky diodes, pyroelectric detectors, and thermopile detectors.^[20] Since the 1990s, superconducting hot-electron bolometers (HEBs) have been developed as fast, very sensitive detectors that are particularly useful for heterodyne detection.^[21] In recent years, substantial advances for rectifiers based on field-effect transistors utilizing plasmonic effects^[22] as well as for microbolometers and nanobolometers have been achieved.^[23] A comprehensive review on the state of the art regarding THz detectors in general has been presented in the recent article by Sizov.^[24] The role of 2D materials in the field of photodetection in the spectral range from THz to UV light has been summarized,^[25] and there is a tutorial on graphene-based materials for THz detection.^[26] A detailed review of infrared and THz detector concepts and properties can be found in the review article by Rogalski et al.^[27] In particular, many different materials suitable for near-infrared detection are discussed here. Wang et al. review progress and challenges of THz detectors based on 2D materials.^[28] In the following, we present various detection mechanisms and key parameters. In addition to the main routes of THz detection in 2D materials that are covered in previous reviews,^[25,27,28] we also discuss unconventional detectors that are uniquely enabled by 2D materials, in particular in Section 2.2.4, 2.2.5, and 2.5.

When assessing and comparing THz detectors there are several important figures of merit, which are summarized in **Table 1**. Often these measures are interrelated and competing—the most sensitive detectors may lack the output bandwidth, for example. There are additional unquantifiable factors that must be considered, including cost and ease of fabrication, and compatibility with manufacturing technologies.

Detectors based on 2D materials exploit a diverse range of physical mechanisms and they are optimized for different key parameters, such as low noise-equivalent power (NEP), large spectral bandwidth, or high temporal resolution corresponding to high electronic bandwidth. In Section 2.2, we explain the basic physical principles of the most widely employed detection mechanisms. After that, two sections focus on optimized detectors for either low-noise operations or for high-speed operation.

Table 1. Important figures of merit for photodetectors.

Quantity	Symbol	Unit	Definition
Responsivity	R	$A W^{-1}$ or $V W^{-1}$	Measured electric signal divided by incoming radiation power
Noise-equivalent power	NEP	$W Hz^{-0.5}$	Incoming power for which a signal-to-noise radiation of one is obtained at output bandwidth of 1 Hz
Output bandwidth	BW	Hz	Electronic bandwidth on output side
Specific detectivity	D^*	$1 cm Hz^{0.5} W^{-1} = 1 \text{ Jones}$	$D^* = (A \cdot BW)^{0.5} / \text{NEP}$, where A is the detector area
Dynamic range	DR	Dimensionless	Ratio between the power at which the detector saturates and the minimum detectable power

Finally, detection integrated into near-field microscopy and devices for time-resolved THz sampling, respectively, are presented. **Figure 3** illustrates the most common THz detection principles and the underlying physics.

2.2. Detection Mechanisms in Devices Based on 2D Materials

In the following, we focus on the main mechanisms and concepts that are exploited in devices with specified detector parameters. In addition to these mechanisms also THz photocurrents based on the photogalvanic and photon drag effect have been verified experimentally.^[29] Furthermore superconductor-graphene-superconductor junctions have been proposed for THz detection^[30] and first experimental demonstrations have been reported.^[31]

Note that multiple detection mechanisms discussed in the following sections may occur simultaneously in a single device. Often it is not easy to disentangle the contributions from different mechanisms. In a recent joint experimental and theoretical study of detection in a graphene-based field effect transistor operated at different temperatures, the contribution of the photothermoelectric effect, pn-junction rectification, and plasmonic rectification in the sub-THz frequency (0.13 THz) response was clarified.^[32] Also for field-effect transistors (FETs) based on black phosphorus the role of plasma-wave related rectification, photothermoelectric response and bolometric response have been disentangled.^[14b,33]

Many detectors utilizing 2D materials are realized in the form of FETs. Bolometric and photothermoelectric detectors by nature are two-terminal devices. If they are fabricated in form of FETs the radiation is typically coupled in via the source and

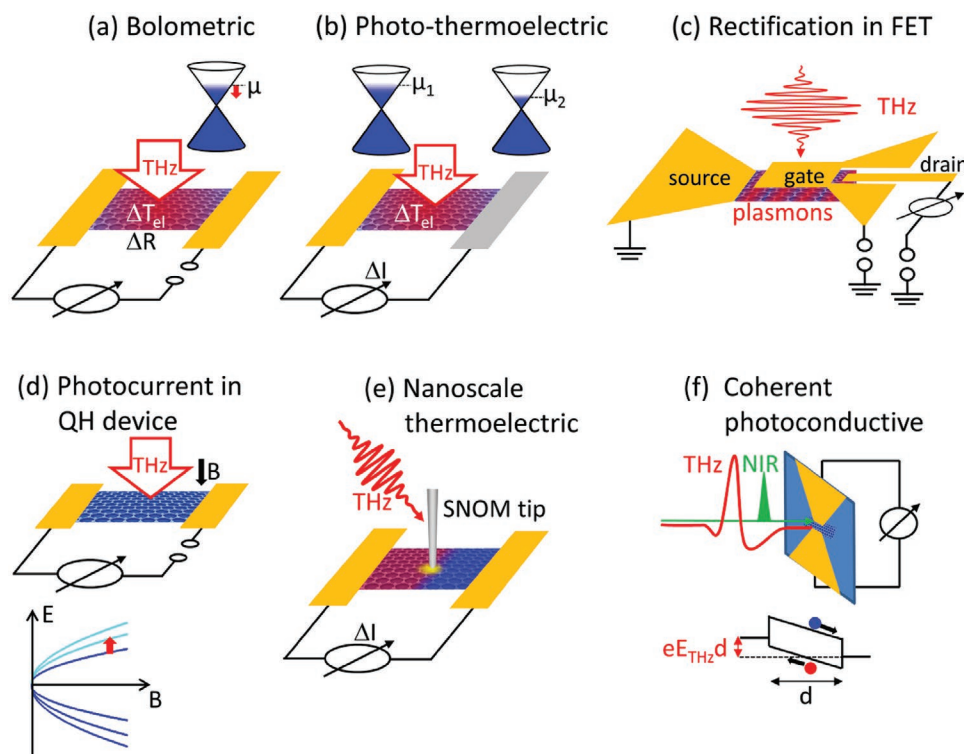


Figure 3. In the first row a–c) the most common principles for THz detection in 2D materials are depicted. In the second row d–f) more unconventional detectors that are also discussed in this article like a quantum Hall (QH) device and local detection in scanning near-field optical microscopy (SNOM) are shown. All these techniques measure the intensity of THz radiation, while coherent photoconductive detection (f) records the THz field in the time domain.

drain contacts and the electric signal is measured at the same contact pair. Note, however, that an antenna design utilizing source and gate contacts for THz coupling is also attractive for photo-thermoelectric detection.^[14b] The additional gate electrode allows one to optimize the detector performance by controlling the carrier density in the 2D material. Rectifying detectors based on 2D materials are also designed as FET structures. Here, however, the radiation is coupled in via the source–gate contact pair. The detector signal is again measured via the source–drain contacts.

As a final general remark, detectors of micrometer size require an antenna for efficient incoupling of THz radiation with wavelengths much larger than the device size.^[34] Alternatively, large-area detector designs have been proposed and developed.^[14a,35] Broadband antennas such as bow-ties, logarithmic spirals, or logarithmic-periodic antennas enable large spectral bandwidth while resonant antennas such as dipoles can utilize higher responsivity and NEP at particular frequencies. Similarly, the large-area electrode structures can be fabricated for either broadband operation or resonant enhancement.

2.2.1. Bolometric Detectors

A bolometer consists of an absorbing layer on a material that changes its resistance upon changes of temperature (cf. Figure 4). It is coupled through certain thermal conductance to a thermal reservoir. For high sensitivity, a strong temperature dependence of the resistance R expressed by the coefficient $\alpha = R^{-1} \cdot (dR/dT)^{-1}$ is desirable. Furthermore, a low heat capacity C of the bolometer material and a low thermal conductance G of the connection to the reservoir are beneficial for achieving large responsivities. For fast operation, on the other hand, the thermal conductance should be large. The response time is determined by the thermal time constant $\tau_{th} = C/G_{eff}$, where G_{eff} is the effective thermal conductance considering all channels of heat losses.

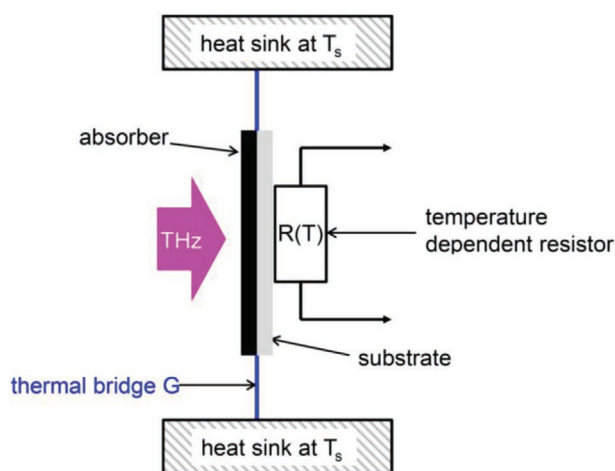


Figure 4. Schematic representation of the layout of a bolometric detector. A bolometer that practically contains these components separately is called composite bolometer. For a hot-electron bolometer the electron gas serves as the absorption layer and temperature dependent resistor. Phonons provide the energy transfer for rapid cooling of the electronic system.

The potential of integration in 2D stacks and gating has made graphene an attractive candidate for realizing perfect absorption at certain THz frequencies, that can be tuned by the gate voltage.^[36] Utilizing these novel absorbers in bolometers seems highly attractive, however, to our knowledge no such devices have been realized so far. Novel nanomechanical bolometers based on graphene and MoS₂ have been recently demonstrated for near-infrared detection.^[37] Here a mechanical transduction resulting in a change of resistivity is used for measuring the temperature. This concept for flexible, room-temperature devices that are interesting for wearable electronics is expected to be functional also at THz frequencies.

Let us consider now a graphene-based HEB. In such a detector, most components of a bolometer are contained within the doped graphene layer. The energy of the incoming THz radiation is transferred into internal energy of the electron gas via Drude absorption. The heat capacity of the electronic system is low, resulting in a comparably strong change in electron temperature. Heating the electron distribution results in a broadening of the Fermi edge. Because the density of states rises linearly with energy in graphene and because the THz radiation does not change the number of carriers in the doped graphene layer, this broadening causes a lowering of the chemical potential μ .^[38] In turn, the total contribution of interband absorption increases (cf. Figure 5). Required by sum-rule considerations, the Drude absorption part has to decrease accordingly. The reduced DC conductivity delivers the output signal of the HEB. The electron gas cools rapidly on the picosecond scale by transferring energy to the graphene lattice.^[38,39] The main cooling process here is scattering via optical phonons, thus, the response of a HEB can be ultrafast. In other 2D materials like black phosphorus similar bolometric effects occur. However, due to the bandgap, moderate doping will not result in a Fermi energy in the conduction band (or valence band for p-type material) as in the case of graphene. Rather the Fermi energy will be localized between the donor (acceptor) levels and the band edges. For suitable binding energies the temperature dependence of the number of extrinsic carriers in the bands facilitates the bolometric effect.

Next, we present two examples of graphene-based HEBs operated at room temperature. For the first one, a chemical vapor deposition (CVD)-grown graphene flake is transferred

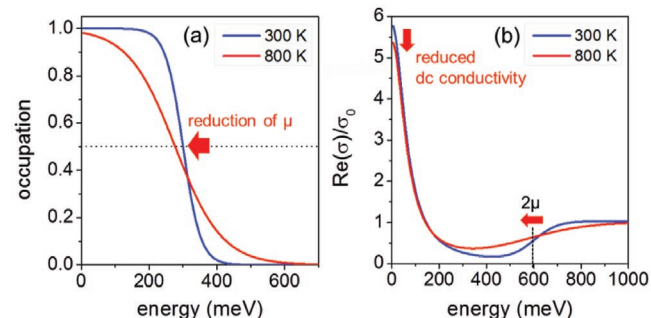


Figure 5. Illustration of the bolometric effect in graphene: Conservation of the number of charge carriers results in a lowering of the chemical potential a). This lowers the onset energy for interband absorption and due to sum rule requirements lowers the intraband absorption b). Here the real part of the dynamic conductivity is plotted, which is proportional to the absorption. Reproduced with permission.^[175] Copyright 2017, Wiley-VCH.

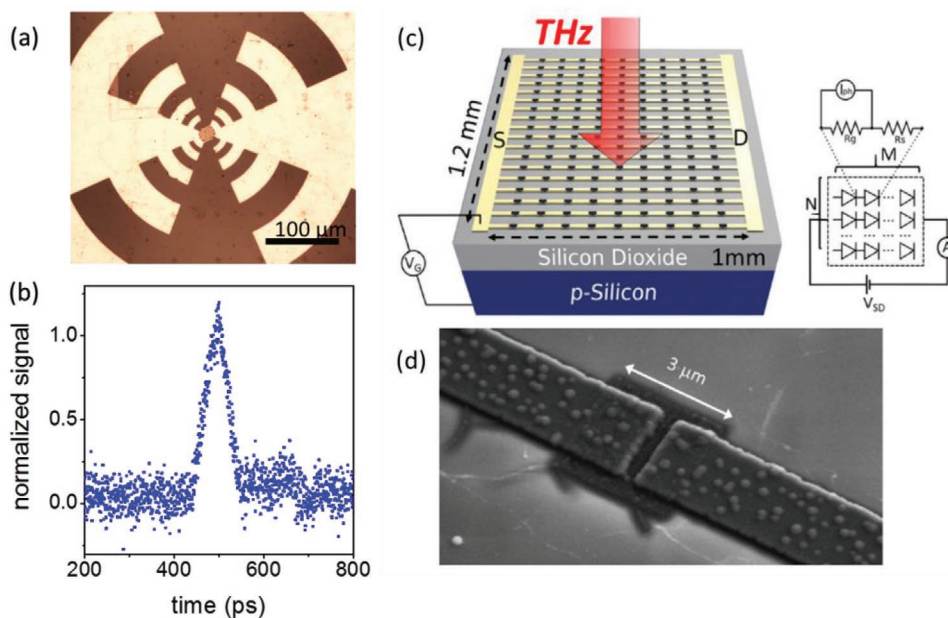


Figure 6. Layout a) and detector response to a short radiation pulse b) of an antenna coupled two-terminal HEB based on a CVD-grown graphene layer transferred to SiC and coupled to a broadband antenna. Reproduced with permission.^[175] Copyright 2017, Wiley-VCH. Graphene-based HEB fabricated in the form of a large-area plasmonic array. Principle detector structure c) and scanning electron micrograph d) of a small unit, showing the contacted graphene. Reproduced under the terms of the Creative Commons Attribution 3.0 licence.^[35] Copyright 2017, IOP Publishing.

to a SiC substrate and coupled to a broadband logarithmic-periodic THz antenna. This ultra-broadband detector covers the full range from THz radiation to visible light without any gap.^[40] The signal rise time is 40 ps, limited by the electric circuitry (cp. **Figure 6b**). The second example makes use of a large-area design instead of an antenna. Microstructured CVD-grown graphene rectangles on a Si/SiO₂ substrate are contacted with source and drain contacts that are patterned in form of a plasmonic antenna array (cp. **Figure 6c,d**). This means that at the resonant frequency of ≈ 2.3 THz, enhanced THz fields are coupled from the ends of the metallization stripes into the graphene patches. With this detector very high responsivity values of 2 mA W⁻¹ have been achieved.^[35]

Hot-electron bolometers are also well suited for heterodyne detection. A mixer based on large-area neutral graphene on SiC operated at low temperature features outstanding noise temperatures, i.e., just a factor of two above the quantum limit $\hbar\omega/k_b$.^[41] Such detectors can be employed in heterodyne receiver systems for astronomy applications.

2.2.2. Photothermoelectric Effect

In asymmetric junctions of materials with different Seebeck coefficients a voltage in the circuit is induced when the two junctions are situated at different temperatures. Even in symmetric junctions it is possible to generate a voltage when a temperature gradient within the junction exists. This thermoelectric effect is exploited in photothermoelectric detectors, also called thermopile detectors if they feature multiple junctions. Since materials like graphene and black phosphorus exhibit large Seebeck coefficients (graphene: ≈ 100 $\mu\text{V K}^{-1}$, depending on doping level and mobility^[42]), comparable strong signals can

be obtained. The Seebeck coefficient S can be calculated via the Mott formula by evaluating derivative of the conductivity σ with respect to the energy ε in the vicinity of the chemical potential μ . For the case $k_B T_{el} \ll \mu$ one can apply the Sommerfeld expansion and obtains^[43]

$$S = - \frac{\pi^2 k_B^2 T_{el}}{3e} \left. \frac{1}{\sigma} \frac{\partial \sigma}{\partial \varepsilon} \right|_{\varepsilon = \mu} \quad (5)$$

In **Figure 7a**, photothermoelectric detector, comprising Cr-graphene and Au-graphene contacts, is depicted. The lateral distribution of electron temperature, Fermi energy, Seebeck coefficient and the potential gradient are also shown in **Figure 7h–j**. The detector signal is given by the potential gradient integrated along the x -direction, i.e., the area underneath the curve presented in **Figure 7k**. Highest detector responsivity R was obtained when the graphene sheet was operated close to charge neutrality. This is in accord to theoretical considerations indicating that $R \approx (\mu\sigma)^{-1}$. Since this type of photothermoelectric detector, similar to the bolometric detectors discussed above, utilizes the electron temperature rather than the lattice temperature, it is capable of ultrafast operation. For example, the detector presented here can provide electrical output signals with a full-width at half maximum of 30 ps, again limited by the electric circuitry.^[14a]

Apart from graphene, black phosphorus has also been successfully applied in photothermoelectric detectors.^[14b,33b,44] It has been shown that 30–40 nm thick multilayer black-phosphorus has ideal properties with respect to tunability of the carrier concentration for THz detection via the photothermoelectric effect.^[44b] Unlike graphene, black phosphorus exhibits anisotropic electrical transport properties due to its structural anisotropy. Thus, in an optimized device the contacts are oriented according to the crystallographic directions.^[44b]

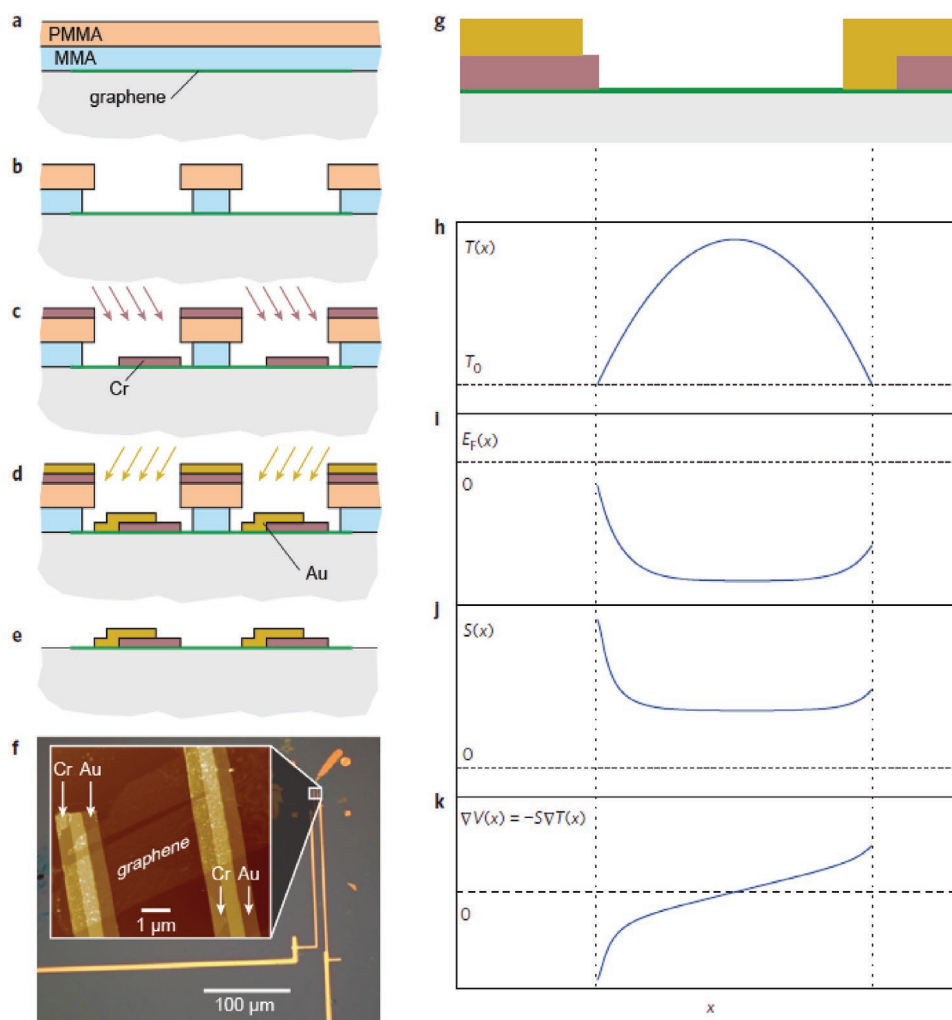


Figure 7. Graphene-based photothermoelectric detector. Parts a–e) show the steps in fabricating a lateral detector featuring graphene–Cr and graphene Au contacts. f) Optical micrograph and atomic-force microscopy image (inset) of the device. g–k) The local distribution of electron temperature T (h), Fermi energy E_F (i), Seebeck coefficient S (j), and the potential gradient $\nabla V(x)$ (k). Reproduced with permission.^[14a] Copyright 2014, Springer Nature.

2.2.3. Rectification

Rectifying detectors are based on a nonlinear electric response. Common devices are Schottky diodes and FETs that can be operated at room temperature. As mentioned earlier, the THz alternating field is coupled to the source–gate contact pair via an antenna. The field results in a periodic modulation of the carrier density in the channel. This modulation of the carrier concentration together with the applied alternating field leads to a rectification effect that can be monitored by a change of source–drain DC current. Interestingly, this rectification effect can be exploited at frequencies far above the cutoff frequency related to the gain of the transistor.

The high frequency operation is enabled by a plasma wave mechanism proposed by Dyakonov and Shur.^[45] The 2D electron gas in a FET can sustain plasma waves that are excited via the THz field coupled to the source contact. Depending on the parameters of the transistor, different regimes can be distinguished. In the weakly damped regime, also called resonant regime, the plasma wave can travel from the source to the drain contact and

is reflected there. Thus, standing waves can be formed in the transistor channel that acts as a cavity. In this regime, the response can be resonantly enhanced by a factor of 5–20.^[45b] The weakly damped regime requires the transit time of the plasma wave through the channels to be shorter than the momentum relaxation time. In the more commonly used overdamped regime, on the other hand, plasma waves decay before they reach the drain. Thus, modulation takes place only in the part of the channel close to the source contact. This regime enables broadband detection.

Note that this is only a very coarse classification of FET rectifiers. Depending on detector design and applied voltages numerous more subtle modes of operation can be distinguished. These are beyond the scope of our review, in particular because they are rarely discussed in publication on FETs based on 2D materials. Readers interested in details are referred to review articles by Knap et al.^[46] and by Otsutji.^[22]

The first rectifying detectors utilizing 2D materials were fabricated on exfoliated monolayer or bilayer graphene flakes,^[34b,47] while successive technology used materials that are more compatible with industrial production such as epitaxial graphene on

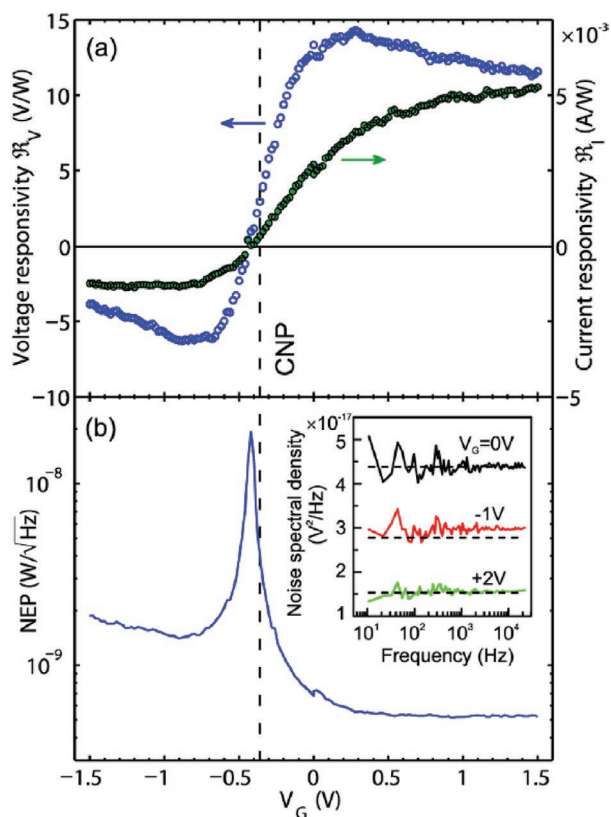


Figure 8. Detector responsivity a) and NEP b) of FET based on CVD-grown graphene irradiated with 0.6 THz radiation. Reproduced with permission.^[34c] Copyright 2014, American Chemical Society.

SiC^[48] or CVD-grown graphene.^[34c,49] The detector performance has undergone considerable improvement, in particular by appropriate antenna design and impedance matching to the detector. As an example, impressive responsivity and NEP data for the first FET utilizing CVD-grown graphene are presented in **Figure 8**.

In black phosphorus larger on-off ratios of the transistors as compared to graphene are feasibly due to the presence of a bandgap. Among other mechanisms, rectification via plasma waves has been exploited for THz detection in black-phosphorus-based FETs.^[50]

Rectifiers using 2D materials most often are designed as FETs making use of the plasma wave mechanism described by Dyakonov and Shur. However, recently rectification at lateral Schottky junctions has also been reported.^[51] In fact, for that particular device the rectification at the Schottky junctions results in a higher responsivity as compared to the plasma wave mechanism.^[51] Another way of utilizing rectification with Schottky contacts has been realized in detectors where graphene serves as a metal layer and n-doped SiC as the semiconductor material.^[52] This Schottky rectifier with epitaxially defined interface is connected to a logarithmic periodic antenna.

2.2.4. Plasmonically Enhanced Detection

We have already mentioned plasmonic effects with regard to an enhanced incoupling of radiation into a bolometric detector

mediated by micropatterned metal lines. Furthermore, plasmonic effects within the 2D materials are exploited in most rectifying detectors based on these materials. Typically evidence for these plasmonic effects can be only obtained indirectly by comparing the detector performance with simulation results. Recently Bandurin et al. fabricated an antenna-coupled FET, where bilayer graphene is sandwiched between two h-BN layers.^[53] The device realizes a plasmonic Fabry–Perot cavity and clear resonant peaks can be directly observed in the measured responsivity at low temperature (10 and 77 K).^[53]

Another way of utilizing plasmonic effects within 2D materials is to pattern doped layers into ribbons.^[19,54] By controlling the doping level as well as the width and periodicity, plasma oscillations can be excited when the ribbons are excited with radiation polarized perpendicular to the ribbon lines. As a result, resonantly enhanced absorption occurs at frequencies in the vicinity of the plasma frequency. For example, a bolometric detector based on 140 nm wide graphene nanoribbons has been demonstrated.^[55] Via tuning the gate voltage the carrier concentration was tuned in order to match the plasmon frequency to 28 THz, which was the frequency of the incident radiation. The achieved photocurrents increased by a factor of up to 15 for radiation polarized perpendicularly to the ribbons, i.e., addressing the plasmonic response, as compared to radiation polarized along the ribbons, which exploits the weaker free-carrier (Drude) absorption. For the frequency range 2–10 THz a photothermoelectric detector utilizing 2.3 μm wide graphene ribbons has been demonstrated.^[56]

2.2.5. Landau Level Enhanced Detection

A device that exploits photoconductivity in the quantum Hall regime has been developed by Kawano.^[57] This detector is ultra-broadband and its spectral responsivity can be tuned by the magnetic field. When a magnetic field is applied perpendicular to the graphene layer, Landau quantization sets in and the linear dispersion is split into a series of Landau levels (LLs). Their energy E_n scales with the square root of the magnetic field B as $E_n = \pm v_F \sqrt{2e\hbar B |n|}$, where n is the LL index and $v_F \approx 10^6 \text{ m s}^{-1}$ the Fermi velocity (cf. Figure 3d). In a conventional semiconductor with parabolic dispersion, on the other hand, E_n depends linearly on B with the slope being determined by the effective mass m^* as described by $E_n = (eB/m^*) \hbar(n + 1/2)$.

Upon irradiation with THz radiation with powers in the μW range, detector signals were obtained when the photon energy was resonant with the LL spacing. Due to the square root dependence of E_n on B a large tuning range from 0.76 to 33 THz was achieved for the graphene-based detector for magnetic fields below 5 T. A reference detector based on a 2D electron gas in GaAs exhibited resonant enhancement only for the range from 0.76 to 1.6 THz, for the same span of magnetic fields.

Partly along the same lines a detector based on gatable free-standing graphene in a magnetic field has been demonstrated for near infrared radiation.^[58] For this detector a very large responsivity of 0.13 A W^{-1} , corresponding to 17 electron–hole pairs per incident 100 photons, was measured. Sonntag et al.

attribute this to carrier multiplication^[59] at the edges, where the photogenerated electrons and holes of the quantum Hall edge channels are reflected.^[58] Since the proposed mechanism does not depend on photon energy, similar devices should be functional in the mid-infrared and THz range. Rapid thermalization of the Landau-quantized electronic system via Auger scattering^[60] should furthermore enable fast detector response times.

2.3. Highly Sensitive Detectors

Shortly after the discovery of graphene various THz detectors have been proposed theoretically^[61] and outstanding values of $R \approx 200 \text{ V W}^{-1}$ and $D^* \approx 10^9$ Jones have been predicted.^[61b] Experimental realizations of detectors based on 2D materials have undergone a rapid development from the first demonstrations to devices with competitive parameters summarized in **Table 2**. The most widely used materials are monolayer and bilayer graphene. However, in recent years a number of detectors based on black phosphorus have emerged and also MoSe_2 , belonging to the class of TMDCs, has been explored. Graphene-based detectors have rapidly progressed from devices utilizing exfoliated flakes^[34b,47] to devices using large-scale graphene that is suitable for industrial production such as CVD grown graphene^[34c,49] or epitaxial graphene on SiC.^[48] Furthermore flexible graphene-based detectors^[62] have been developed that may find application in novel systems, such as wearable THz spectrometers and communication devices.^[63]

Hot-electron bolometers based on graphene quantum dots operated at cryogenic temperatures have reached very low NEP values of $2 \times 10^{-16} \text{ W Hz}^{-0.5}$ (based on absorbed power).^[64] A limitation of these detectors is the practically nonexistent dynamic range for linear detection. It is caused by the decline of responsivity with incident THz power that occurs already at the lowest investigated power levels.^[64a] Note that the NEP is still orders of magnitude higher than the NEP of superconducting hot-electron bolometers.^[23b] Many 2D materials also become superconducting at low temperatures. Hot-electron bolometers based on magic-angle bilayer graphene provide spectrally resolved single photon detection in the THz range.^[65]

With respect to dynamic range, superconducting bolometers feature similar limitations as the graphene quantum dot device. Clearly the main interest using 2D materials arises for room-temperature operated devices. Generally, most devices optimized for frequencies below ≈ 0.5 THz exploit the rectification mechanism associated with plasma instabilities. Devices for higher frequencies often are photothermoelectric detectors (cf. Table 2). Responsivity and NEP values are typically around the range of few V W^{-1} and $\text{nW Hz}^{-0.5}$, respectively. Similar NEP values are reached by the best commercially available pyroelectric detectors, though most commercial detectors exhibit much larger NEP values.^[24] Furthermore, the best values achieved for devices based on 2D materials in the $10 \text{ pW Hz}^{-0.5}$ range are approaching the record values reported for Si FETs and VO_2 -based microbolometric detectors.^[24]

Note that the comparison of NEP values for different detectors is not always unambiguous. Whenever possible, we cite values considering the power of the incoming radiation instead

of the absorbed power. In many studies, the experimentally determined NEP value is an upper limit that may be determined by the readout devices connected to the detector. In other studies, the NEP values are concluded from measured responsivity data and theoretical considerations concerning the detector noise. This approach provides a lower limit to the NEP as there may be sources of noise in the actual device that are not considered in the idealized theoretical description.

2.4. Room Temperature Fast Detectors

As discussed previously, basically all important detection mechanisms in 2D materials occur on ultrafast timescales of a few ps. Furthermore, the mechanisms are suitable for room temperature operation. The responsivity of rectifying mechanisms drops toward higher frequencies due to intrinsic time scales and due roll-off related to RC-time constants. The bolometric and photothermoelectric effect, on the other hand, are by nature broadband. In summary, these physical properties make 2D materials ideal for fabrication of detectors featuring fast response times at room temperature. Such fast detectors are of interest for many purposes. For example, ultrafast low-noise THz receivers are ideal for heterodyne detection. Broadband fast detectors, on the other hand, are very valuable for timing purposes in time-resolved multicolor experiments. Photothermoelectric detectors based on graphene^[14a] have reached NEP values that are competitive with Schottky diodes that have undergone long optimization processes. Notably the detectors based on 2D materials cover a wide spectral range. For graphene-based HEBs it has been shown that a single detector element can cover the range from sub-THz to visible light.^[40] Because these detectors are not optimized for any resonant frequency, their NEP is rather large. Nevertheless, their NEP is comparable with silicon-based broadband photon-drag detectors. Furthermore the temporal resolution of the graphene based HEB is about 20 times superior to those photon-drag detectors.

2.5. Nanoscale Detection

Because of the long wavelength, far-field detection of THz radiation is accompanied by low spatial resolution. For example, focusing radiation of frequency of 1 THz with high numerical aperture will result in a spot size of about $150 \mu\text{m}$. Near-field microscopy, on the other hand, allows spatial resolutions far beyond the Abbe diffraction limit. THz nanoimaging and nanospectroscopy is possible via scattering-type near-field optical microscopy (s-SNOM). In this technique, a sharp metal tip on a cantilever of an atomic force microscope, which is raster scanned across the sample surface, is illuminated by THz radiation. Collecting the (back-)scattered radiation from the tip and demodulating the signal at harmonics of the cantilever oscillation frequency provides access to near-field information. Thus, detectors employed in s-SNOM need to be able to record signals at the cantilever harmonics that are typically in the few 100 kHz range. The near-field signals contain information on the local dielectric function of the material underneath the

Table 2. Detector parameters for detectors based on 2D materials and a few references for state of the art detectors not based on 2D materials (lower part). GFET: graphene-based field-effect transistor, BP: black phosphorus, HEB: hot-electron bolometer, HEMT: High-mobility electron transistor.

Detector type	Operation temperature	Frequency	Responsivity	NEP	Reference, year
Graphene quantum dot HEB	2.5 K	THz–UV	10^{10} V W^{-1} based on absorbed power	$2 \times 10^{-16} \text{ W Hz}^{-0.5}$ based on absorbed power	[64a], 2018
Plasmonic resonator FET	10 K	2 THz	200 V W^{-1}	$2 \times 10^{-16} \text{ W Hz}^{-0.5}$	[53], 2018
GFET, plasmonic and photothermoelectric	300 K	0.8 THz	535 V W^{-1}	$< 2 \times 10^{-10} \text{ W Hz}^{-0.5}$	[48a], 2018
Lateral Schottky rectifier on graphene	300 K	0.129 THz 0.45 THz	15 V W^{-1} 3 V W^{-1}		[51], 2018
Flexible GFET	300 K	0.487 THz	2 V W^{-1}	$3 \times 10^{-9} \text{ W Hz}^{-0.5}$	[62], 2017
Bilayer GFET	300 K	0.3 THz	30 V W^{-1}	Estimated $1.6 \times 10^{-10} \text{ W Hz}^{-0.5}$	[179], 2017
GFET	300 K	0.4 THz	74 V W^{-1}	Calculated $1.3 \times 10^{-10} \text{ W Hz}^{-0.5}$	[180], 2017
Graphene photovoltaic	300K	2 THz	$34 \mu\text{A W}^{-1}$	$1.5 \times 10^{-7} \text{ W Hz}^{-0.5}$	[181], 2016
Bilayer GFET on SiC	300 K	0.3 THz	0.25 V W^{-1}	$8 \times 10^{-8} \text{ W Hz}^{-0.5}$	[48b], 2015
Graphene photothermoelectric	300 K	2 THz	4 V W^{-1}	$2 \times 10^{-9} \text{ W Hz}^{-0.5}$	[161], 2015
GFET (CVD grown)	300 K	0.237 THz	0.1 V W^{-1}	$10^{-5} \text{ W Hz}^{-0.5}$	[49], 2015
GFET (CVD grown)	300 K	0.6 THz	14 V W^{-1}	$5 \times 10^{-10} \text{ W Hz}^{-0.5}$	[34c], 2014
Large area graphene photo-thermoelectric	300 K	2.5 THz	10 V W^{-1}	$10^{-9} \text{ W Hz}^{-0.5}$	[14a], 2014
Plasmonic monolayer GFET	300 K	0.3 THz	$1 \times 10^{-6} \text{ V W}^{-1}$	$2 \times 10^{-7} \text{ W Hz}^{-0.5}$	[34b], 2012
Plasmonic bilayer GFET	300K	0.3 THz	$6 \times 10^{-2} \text{ V W}^{-1}$	$3 \times 10^{-8} \text{ W Hz}^{-0.5}$	[34b], 2012
Thermoelectric BP detector	300 K	3.4 THz	3 V W^{-1}	$7 \times 10^{-9} \text{ W Hz}^{-0.5}$	[44b], 2019
BP phototransistor	300 K	$< 0.14 \text{ THz}$	$< 0.3 \text{ V W}^{-1}$	Estimated $10^{-10} \text{ W Hz}^{-0.5}$	[33a], 2018
BP photoconductor	300 K	0.15 THz	300 V W^{-1}	Calculated $10^{-10} \text{ W Hz}^{-0.5}$	[182], 2017
BP Photoconductor	300 K	2.5 THz	10^{-3} V W^{-1}	$1.3 \times 10^{-4} \text{ W Hz}^{-0.5}$	[44a], 2017
BP plasmonic FET	300 K	0.28 THz	0.14 V W^{-1}	$10^{-7} \text{ W Hz}^{-0.5}$	[50], 2015
MoSe ₂ FET	300 K	0.29 THz	$3.8 \times 10^{-2} \text{ V W}^{-1}$	$6.6 \times 10^{-6} \text{ W Hz}^{-0.5}$	[183], 2016
For comparison: Detectors not based on 2D materials	Operating temperature	Frequency	Responsivity	NEP	Reference, year
Superconducting HEB	100 mK	Broadband		$10^{-19} \text{ W Hz}^{-0.5}$	[23b], 2011
Ge:Ge unstressed	1.65 K	$\approx 2.3\text{--}3.8 \text{ THz}$	$\approx 10 \text{ A W}^{-1}$	$2.1 \times 10^{-17} \text{ W Hz}^{-0.5}$	[184], 2010
Ge:Ge stressed	1.65 K	$\approx 1.3\text{--}2.3 \text{ THz}$	$\approx 40 \text{ A W}^{-1}$	$8.9 \times 10^{-18} \text{ W Hz}^{-0.5}$	[184], 2010
Pyroelectric, LiTiO ₃	300 K	0.2–30 THz	30 V W^{-1}	$4 \times 10^{-10} \text{ W Hz}^{-0.5}$	[185], 2011
Microbolometer, VO _x	300 K	1.5–100 THz		$(2\text{--}3) \times 10^{-11} \text{ W Hz}^{-0.5}$	[186], 2012
Si FET	300 K	0.295 THz	10^5 V W^{-1}	$\approx 2 \times 10^{-11} \text{ W Hz}^{-0.5}$	[187], 2011
InAlAs/InGaAs/InP HEMT	300 K	0.2 THz	$2 \times 10^4 \text{ V W}^{-1}$	Calculated $4.8 \times 10^{-13} \text{ W Hz}^{-0.5}$	[188], 2014

tip.^[66] The spatial resolution of an s-SNOM is independent of the employed wavelength and is determined by the radius of the cantilever tip.^[67] Typical values are a few tens of nm.

Research highlights on 2D materials and related systems include the visualization of plasmonic interferences at graphene edges and at defects.^[68] Furthermore, black phosphorus has been investigated in a novel self-detection scheme, where a quantum-cascade laser is employed as a source and at the same time serves as a THz detector device.^[69] Very recently, the optical constants of surface states in topological insulators were determined in a s-SNOM study without assuming a particular model for the spectral response.^[70]

The efficient detection mechanisms discussed in the above sections have led to a novel combination of s-SNOM with local detection in graphene. To this end, mid-infrared radiation was

coupled locally to an electrically contacted graphene sheet via an s-SNOM tip. Measuring the photocurrent at the source–drain contacts, while scanning the tip across the graphene sheet, creates a map of local detection via the photothermoelectric mechanism. Here the local difference in Seebeck coefficients stem from grain boundaries and charge puddles in graphene.^[71] The local detection technique based on the photothermoelectric effect was exploited also in a study to observe propagating plasmons in graphene.^[72] In this experiment defined areas of the graphene layer were electrically back-gated at different potentials in order to achieve well defined local *pn*-junction. Interference fringes in the local photocurrent map revealed information on the propagating plasmons, cf. **Figure 9**.^[72]

Both studies^[71,72] were carried out with 28 THz radiation from a CO₂ laser. Since both the s-SNOM technique and the

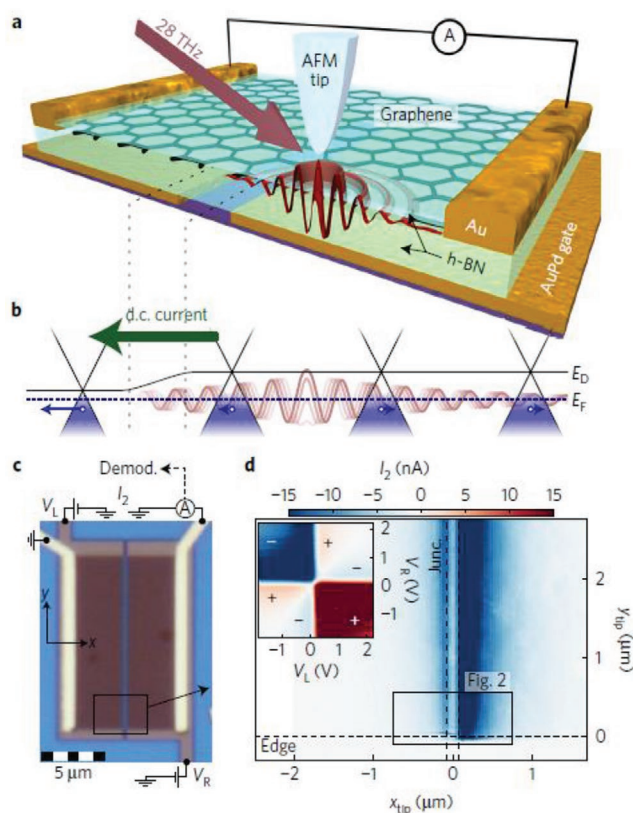


Figure 9. Schematic representation of the combination of s-SNOM and local detection via the photothermal effect a) and the microscopic scheme of this mechanism b). Optical micrograph c) and photocurrent map d) of the device. In the inset of d) the photocurrent upon change of the different gate voltages when the tip is placed at the junction is shown. Reproduced with permission.^[72] Copyright 2016, Springer Nature.

photothermoelectric effect in graphene are ultra-broadband similar studies are enabled also at lower THz frequencies. To this end, resonant tips for THz radiation at the frequency 3.1 THz have been developed and applied in experiments on graphene sheets encapsulated in h-BN.^[73]

2.6. Time-Resolved Sampling with 2D Materials

In Sections 2.1–2.5, incoherent detectors measuring the intensity of the radiation were discussed. In the THz range, time-resolved detectors allow sampling of the electric field of the radiation directly, which offers powerful spectroscopic opportunities. In particular, in time-domain terahertz spectroscopy amplitude and phase of the radiation are measured. Furthermore, coherent detection of THz pulses enables pump–probe experiments with subcycle temporal resolution.

The two most important techniques for coherent detection of THz radiation are photoconductive detection and electro-optic sampling (EOS). The principle of photoconductive THz detection is sketched in Figure 3f. The THz electric field is coupled to the photoconductive material, typically GaAs or InGaAs, via an antenna. When the antenna gap is simultaneously irradiated with an NIR radiation pulse with photon energy above

the bandgap of the material, electron–hole pairs are generated. These carriers get accelerated by the THz field of the radiation, resulting in a measurable photocurrent. In order to sample the THz field in the time domain, the time-delay between THz pulse and NIR pulse are varied. The photoconductive material should exhibit high carrier mobility, but at the same time low (sub picosecond) carrier lifetime. The photocurrent density can be approximated as a convolution of the THz pulse $E(t)$ with the transient carrier concentration $n(t)$ ^[74]

$$j_{ph} = e\mu_c \tau f \int_{-\infty}^{\infty} E(t)n(t-\tau)dt \quad (6)$$

Here e is the electron charge, τ is the carrier lifetime, μ_c is the carrier mobility, and f is the repetition rate of the laser. Low carrier lifetimes are essential to achieve high THz bandwidth and high signal-to-noise ratios.^[75] Materials with bandgaps below 0.8 eV are attractive because they can be operated at the telecom wavelength 1550 nm, where compact fiber lasers are available.

Coherent detection based on graphene has been demonstrated first in a device where both the emitter and detector are integrated on one chip.^[76] For such systems 2D materials are highly attractive since they can be deposited and patterned on arbitrary substrates much easier as compared to the standard low-temperature grown III-V semiconductor epilayers. The THz bandwidth in such systems is limited by the waveguides. Detection of intense free-space THz radiation with graphene-based photoconductive switches showed signals above the noise level at frequencies of about 2 THz.^[77] The attractive feature of this detector is that one can apply any wavelength in the near-infrared to ultraviolet spectral range for gating pulse. Photoconductive detectors based on black phosphorus have been demonstrated by combining exfoliated multilayer black phosphorus with a broadband logarithmic periodic antenna.^[78]

In general, one can expect more work in this direction also with other 2D materials. For example, TMDC materials should have suitable properties like strong NIR absorption at excitonic resonances. Since the carrier dynamics in these systems strongly depends on adsorbed molecules at the surfaces, one may be able to tailor carrier lifetimes by controlling the surface and interface properties.

Regarding EOS for coherent THz detection, 2D materials in general seem less suitable since typically crystals of thicknesses in the 100 μm range are needed. Nevertheless the technique of exfoliation and van der Waals bonding can be also useful for preparing superior EOS crystals. In this respect ultra-broadband etalon free EOS detection has been recently demonstrated by 5 μm GaSe crystals that were van der Waals bonded to a diamond substrate.^[79] The role of the substrate is to delay the internally reflected THz pulse to times beyond the measured range.

3. THz Modulation

Control over the intensity of a radiation source, which is vital for communication in the near-infrared range, is usually accomplished by optoelectronic modulators: an electronic signal is imprinted on an optical carrier, allowing transmission of large amounts of data over long distances. For THz radiation,

modulation so far was mostly important for scientific purposes, e.g., modulation of a THz beam with an optical chopper for lock-in detection. As radio communication is approaching the THz range, the development of highly efficient modulators in this frequency range becomes more urgent. Currently carrier frequencies of several tens of GHz are in use for 5G networks, reaching bandwidth of up to 400 MHz for high speed data transmission.

In the visible and near-infrared range, modulators are most commonly based on electro-optic materials, in which the refractive index can be directly controlled by electric fields. This change in refractive index results in a phase shift of the near-infrared radiation. Combining the phase change with an interferometer enables efficient and fast intensity modulation.^[80] In the THz range, this approach is not feasible as the phase difference that can be achieved with an electro-optic crystal scales inversely to the wavelength. The low photon energy of THz radiation usually does not allow for interband excitation. Even for the few exceptions, e.g., graphene, interband excitation of additional carriers is negligible due to the thermal occupation in the conduction band. Hence, phonon absorption and free-carrier (Drude) absorption dominate the optical properties in many materials. As the latter can be controlled efficiently in 2D electron gases (2DEGs), e.g., via electro-static gating, they are well suited for THz modulators. Though conventional 2DEGs in semiconductor quantum wells have been exploited for THz modulation already, 2D materials add new features as they can be combined with other structures easily. A review dedicated to THz modulators based on 2D materials was recently published.^[81]

The most important figure of merit for modulators is the modulation depth m , that is defined by the degree of change in transmission that can be reached and is usually given in %

$$m = \frac{T_{\max} - T_{\min}}{T_{\max}} \quad (7)$$

The modulation depth for devices working in reflection is calculated in analogy to the transmission. While for many scientific uses the modulation speed, i.e., how fast the carrier can be modulated, is not critical (e.g., for lock-in measurements modulation speed in kHz range is sufficient), for communication purposes a high speed modulation is important. A good figure of merit for the speed of a modulator is the 3dB bandwidth or cutoff frequency, at which m is decreased by 3dB. Besides modulation depth and bandwidth, the THz range in which the modulator works is important to characterize a device, though less well defined. In Section 3.1, we introduce the different mechanisms that can be exploited to modify the optical properties of 2D materials, subsequently the different types of modulators are discussed. Section 3.3 gives a glimpse of more exotic types of THz modulators.

3.1. Controlling the THz Optical Properties of 2D Materials

Controlling the optical properties of a 2D material can be achieved in many different ways, e.g., by changing the temperature, or by applying electric or magnetic fields. While many of those are impractical for actual devices (e.g., applying or changing a strong magnetic field), changing the carrier density

via optical control pulses or electro-static gating can be done fast and efficiently. We will limit our review to the most commonly used effect, i.e., heating of the carriers, optical gating, and electrostatic gating, a sketch depicting these three effects is presented in **Figure 10**. Each of these effects has advantages and disadvantages, e.g., thermal effects of optically pumped hot carriers in graphene can be very fast, but the modulation depth is limited; optical gating can be very efficient, but is a rather slow process.

3.1.1. Optical Pumping (Carrier Generation/Heating)

Optical pumping can have various effects on the 2D material, but also the underlying substrate. With an intense optical pulse, the transmission can actively be varied, making it an all-optical modulator, e.g., by heating the charge carriers via Drude absorption. In graphene, the absorption is proportional to the real part of the complex conductivity, which can be calculated for intraband processes via^[82]

$$\sigma_{\text{intra}} = \frac{2ie^2}{\pi\hbar} \frac{k_B T_{\text{el}}}{\hbar(\omega + i\tau_s^{-1})} \ln \left[2 \cosh \left(\frac{\mu(T)}{2k_B T} \right) \right] \quad (8)$$

The Drude absorption in graphene features a strong nonlinearity: assuming a thermalized carrier distribution, the energy dependent occupation within the Dirac cones can be described by the Fermi–Dirac equation

$$f_{\text{FD}}(E) = \frac{1}{e^{\frac{E-\mu}{k_B T_{\text{el}}}} + 1} \quad (9)$$

in which μ is the chemical potential, k_B is the Boltzmann constant, and T_{el} is the carrier temperature. Heating up this distribution via intraband absorption results in a widened Fermi edge. The density of states in graphene is proportional to the absolute value of the energy and follows the function $D(E) = \frac{2|E|}{\pi\hbar^2 v_F^2}$, where v_F represents the Fermi velocity in graphene. As the number of carriers in the graphene, which can be calculated via $\int_{-\infty}^{\infty} D(E) f_{\text{FD}}(E) dE$, has to stay constant, the chemical potential decreases with increasing temperature.^[38]

Thus the intraband absorption of highly doped graphene decreases when the graphene sheet is heated by an optical pulse. In addition, the electron scattering time, represented by τ_s , can also be temperature dependent. Pump–probe measurements were carried out in the THz range to investigate the nature of this nonlinearity and revealed a fast cool down of the hot carrier distribution in the picosecond range.^[39c,83] This is particularly relevant for other nonlinear effects, e.g., harmonic generation in graphene: here the variation of the carrier temperature has to take place on a timescale shorter than a cycle of the THz field. If this condition is fulfilled, the real part of the complex conductivity varies during a single cycle, leading to significant distortion of the THz field. Exploiting this process, Hafez et al. demonstrated extremely efficient harmonic generation in a single layer of graphene.^[84]

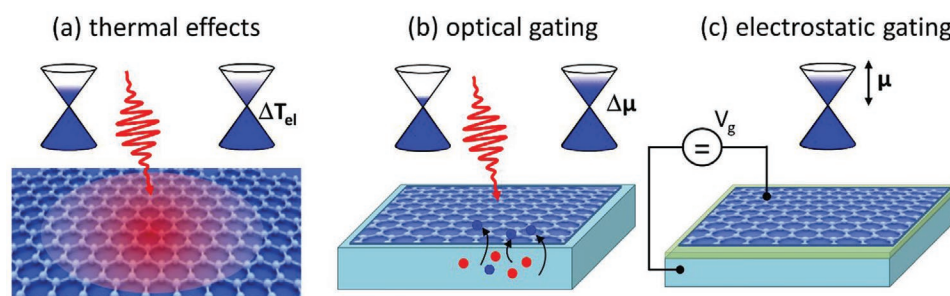


Figure 10. Sketch of different methods to modulate the THz absorption of a 2D material. a) Thermal effects lead to a change in the absorption via a shift in the chemical potential. b) When the 2D material is in direct contact with a semiconductor surface, additional carriers can be introduced by absorption in the substrate. c) Electrostatic gating directly influences the carrier density in the 2D material, and thus the intraband absorption.

Obviously it is of limited use if the control beam and modulated beam have the same frequency. Using a NIR pulse to control the THz properties of a 2D material instead is more appealing for applications. Similar to the degenerate pump-probe experiments, NIR-pump THz-probe experiments can provide insight into the carrier relaxation dynamics. Strait et al. applied this technique to graphene and observed rather slow cooling of the hot carrier distribution at low substrate temperatures.^[85] In the subsequent years, multiple groups investigated the change in THz conductivity of graphene after optical excitation.^[86] The results achieved in those experiments are similar to degenerate THz pump-probe experiments, indicating that the photon energy of the pump beam plays only a minor role: within a picosecond the carrier distribution is thermalized, independently on the original photon wavelength. The hot carrier distribution features a lower Drude absorption, leading to an increased transmission after optical pumping. Further increase of the modulation depth of photoexcited graphene was demonstrated by Weis et al. by combining the graphene layer with a silicon substrate.^[87] In this regime, additional free carriers are mostly generated in the silicon close to the surface, efficiently doping the graphene sheet. A modulation depth of about 80% was reached in a large spectral range with a pump power of 40 mW. Notably, the modulation is inverse to the bare graphene case: optical excitation leads to additional carriers, and thus an increase in Drude absorption. Li et al. demonstrated in 2015 that this effect can be tuned by an additional bias voltage between the graphene layer and the Si substrate.^[88]

For other 2D materials, additional free carriers can be generated optically: in WS₂, for example, interband absorption takes place for photon energies above 1.6 eV.^[89] The introduction of photoexcited carriers leads to an increase in THz absorption in these materials. In contrast to graphene, in which the carrier distribution thermalizes within 1 ps and cools down quickly, the photocarrier lifetime in TMDCs are significantly longer, hence limiting the modulation speed. One important parameter for the carrier lifetime is the substrate of the 2D material: Krishna et al. investigated the role of encapsulation of WS₂ with flakes of hexagonal BN (hBN).^[90] Without encapsulation a THz modulation of 10% was achieved, the carrier lifetime was on the order of 100 ps. Encapsulating quenches the modulation to less than 1%, and simultaneously increases the carrier lifetime significantly, i.e., while encapsulation with hBN is in most cases considered to improve the quality of 2D materials, it can actually

strongly reduce the optical performance in some cases. The role of different relaxation channels in WS₂, e.g., phonon- and defect-assisted relaxation, was investigated by He et al.^[91] They found phonon assisted recombination to be the fastest decay channel for free carriers (≈ 30 ps), while the same processes for excitons is significantly slower (≈ 200 ps). For both, free carriers and excitons, defects lead to slower decay time in the range of 100 ps.

In the same way graphene on Si featured a higher modulation depth,^[87] the interplay between TMDCs and Si can strongly enhance the THz modulation.^[92] When WS₂ is combined with Si, the carriers are mostly generated in the Si close to the surface.^[93] The field offset between the WS₂ and the Si leads to a separation of electrons and holes, leading to a long lived hole population in the WS₂. A high modulation depth beyond 90% is reached under illumination of about 500 mW at 800 nm.^[93a] The separation of electrons and holes that leads to the high modulation depth, also results in a long carrier lifetime on a millisecond scale, limiting the bandwidth of such a device. Only minor modulation of below 10% was observed when the WS₂ was deposited on a sapphire substrate, emphasizing the important role of the substrate. While Yang et al. fabricated their device by liquid-phase exfoliation,^[93a] Chen et al. presented a similar device with MoS₂ directly grown on the Si surface.^[94] With this device a modulation depth of 75% was reached under optical excitation of 0.24 W cm⁻² at a wavelength of 532 nm. A very recent study of MoTe₂ on Si reported a new record modulation depth of nearly 100% when illuminated with 300 mW.^[95]

Using Ge instead of Si as a substrate, the lower bandgap of about 0.6 eV allows for interband carrier excitation at a pump-wavelength of 1.55 μm . Liu et al. presented a broadband modulator reaching around 90% modulation depth at 1 W cm⁻² with MoS₂ directly grown on Ge.^[96]

Other 2D materials offer a more complex THz response after optical pumping: Zhou et al. presented results on Bi₂Se₃ films grown on Al₂O₃.^[97] Interestingly, in this material the THz transmission is quenched in the first few picoseconds after pumping, while after about 10 ps the THz transmission is increased due to a topological phase transition.

3.1.2. Electrostatic Gating

Another way to actively tune the charge carrier density of 2D material is electro-static gating.^[98] The 2D material forms

a capacitor with the underlying substrate, usually a thin SiO₂ layer serves as dielectric material. By applying a voltage across the oxide, the capacitor gets charged by adding or subtracting charge carriers to the 2DEG: the thickness and material of the oxide determine the gate capacitance per unit area C_g . With this the change in carrier density can be calculated via $\Delta n = \frac{C_g V_g}{e}$ from the gate voltage V_g . The Drude model can be exploited to estimate the influence of the additional carriers to the optical properties of the 2DEG. Sensale-Rodriguez et al. proposed in 2011 that graphene could serve as superior gate electrode in combination with conventional 2DEGs in semiconductor quantum wells.^[99] In 2012, Maeng et al. demonstrated gate tuning of the THz properties in a large-area FET.^[100] In contrast to standard graphene FETs that usually have channel lengths on the order of μm or below, a large area is necessary to transmit a THz beam. The sample for this study has a large channel area of $6 \times 6 \text{ mm}^2$ covered with graphene grown by CVD (cf. Figure 11a). Varying the back-gate voltage from -30 to 50 V increased the THz transmission from 82% to 95% in the spectral range from 0.5 to 1.5 THz, corresponding to a modulation depth of about 14% (cf. Figure 11b,c). Later that year, Sensale-Rodriguez also demonstrated a modulator based on the same principle^[13] (cf. Figure 11e). The performance was comparable to the findings of Maeng et al. indicating that this is a natural limit for graphene-based modulators operating in transmission. In addition to the bare characterization of the intensity modulation, Sensale-Rodriguez et al. furthermore measured the cutoff frequency for the modulation. As the active area was high ($15 \times 15 \text{ mm}^2$), the capacity and therewith the RC time constant was rather large, limiting modulation to the kHz range. In 2014, Mao et al. exploited the same type of graphene FET, but instead of the SiO₂, a 60 nm thick film of Al₂O₃ was grown by atomic-layer deposition as dielectric material.^[101] This led to an increase of

the modulation depth of about 22%, and more importantly, a cutoff frequency of 170 kHz was achieved.

Adding an reflective layer on the backside of the Si substrate, the modulation depth can be increased beyond 60%.^[102] The incoming THz wave interferes with the reflected part, maximizing the electric field in the graphene layer. One drawback of this solution is the limitation in THz bandwidth: as the increase in modulation depth is caused by an interference effect, an increase of the modulation depth was only observed in the range of 610–630 GHz. If only a narrow bandwidth is of interest, the substrate thickness can be tailored to this particular frequency. An alternative way to apply a gate voltage for THz devices has been introduced by Gomez-Diaz et al. in 2015: instead of the substrate, a second graphene layer serves as gate electrode.^[103] Two CVD graphene layers were separated by 80 nm of polymethylmethacrylate, that way acting like a single graphene layer that can be gated without further electrodes. This enables the use of an arbitrary, high resistive substrate. Wu et al. made use of this technique and demonstrated a THz modulator based on ionic-liquid gating in a graphene sandwich structure:^[104] two glass slides with graphene layer were stacked together with spacers, the room between the graphene layers was filled with the ionic liquid. With this highly efficient gating, a modulation depth of up to 99% was reached when the gate voltage is varied by 3 V.

Using ionic gel as the electrode material also enables flexible devices. Liu et al. presented a flexible THz modulator based on graphene on a polyethylene substrate with ionic gel for gating on top.^[105] As only one graphene layer was gated, the modulation depth was around 22% when gate voltages of -3 to 3 V were applied. Even after bending the sample for 1000 times leading to a strain of about 1%, the performance is not impaired. Another advantage of the polyethylene substrate is the low reflection, corresponding to an insertion loss of only

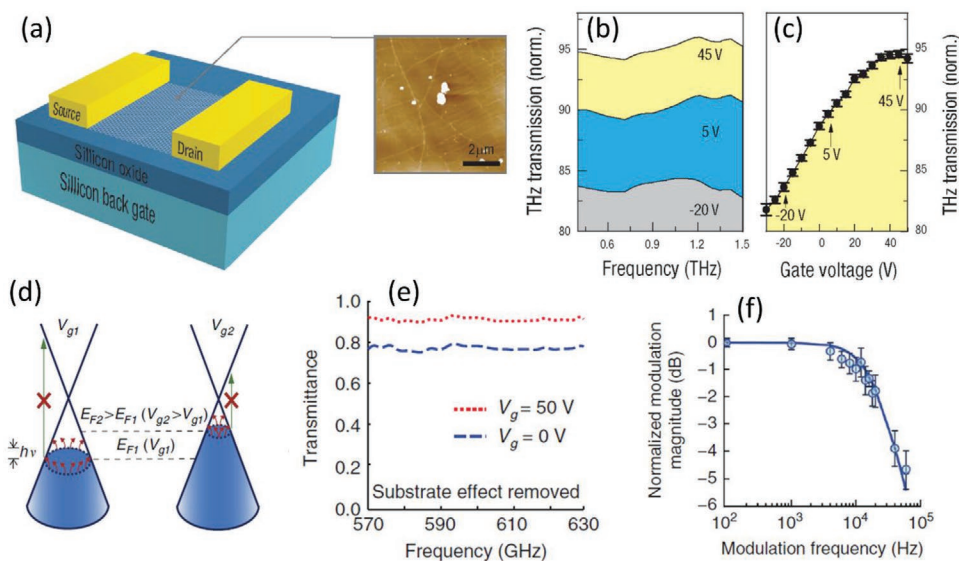


Figure 11. a) Sketch of a large area field effect transistor used for THz spectroscopy on gated graphene, the inset shows an atomic-force microscope image of the channel. b) Transmitted THz spectrum for three different gate voltages. c) Average gate dependent transmission from 0.4 to 1 THz as a function of gate voltage. a–c) Reproduced with permission.^[100] Copyright 2012, American Chemical Society. d) Schema of modulating THz absorption by gating. e) Transmitted spectrum of two gate voltages. f) Normalized modulation depth as a function of modulation frequency. d–f) Reproduced with permission.^[13] Copyright 2012, Springer Nature.

1.2 dB. A combination of the two aforementioned studies was presented by Balci et al.^[106] Two graphene electrodes were applied on a 70 μm thick polyvinyl chloride (PVC) spacer. A modulation depth of 50% was demonstrated for transmission measurements in the microwave range, though the device is also expected to work in the THz. The authors considered this device as switchable radar-absorbing surface: reflection measurements revealed a modulation depth of about 90%, which was further enhanced when combined with an additional spacer and metal film.

3.2. Modulator Geometries

The modulators presented so far are based on transmission or reflection of THz radiation of a 2D material on a substrate, limiting the modulation depth due to the small interaction volume of the THz radiation with a 2D material. Variations of the device geometry can further improve the modulator performance, e.g., by exploiting total internal reflection.^[107] The light-matter interaction can be further increased, e.g., by plasmonic enhancement of the absorption. Smaller, and therewith faster changes of the optical properties of 2D materials can be sufficient to allow for high modulation depth when the THz radiation couples more efficiently to the charge carriers. In this section, we will describe the different techniques that were developed to maximize the light-matter interaction. In general, all control mechanisms discussed in the previous section can be applied to those enhanced modulators.

3.2.1. Hybrid Metamaterials

Probably the simplest way to increase the light matter interaction is the utilization of interference effects caused by a

reflecting surface in the proximity of an absorbing layer.^[108] Tasolamprou et al. reported a photo-induced modulation of the absorbed radiation of about 40% in such a structure.^[109] More complex metamaterials in the vicinity of 2DEGs can be tailored to improve the device performance at certain frequencies:^[110] metal electrodes in the shape of resonator elements, comprised of an inductive and a capacitive part, can be exploited as gate electrodes. By varying the gate voltage, the conductivity in the gap of the resonator is changed, therewith tuning the resonance frequency. This approach has two advantages: shifting the resonance frequency of such structures enables a high modulation depth, furthermore, the small area that has to be gated allows for potentially high speed modulation. A review of such modulators, not limited to 2D materials, was published recently.^[111]

Lee et al. presented the first hybrid metamaterial made from graphene and a hexagonal metal structure.^[112] A sketch as well as a microscope image of the device is depicted in **Figure 12a,b**, respectively. Due to the thick spacer, a rather high voltage of nearly 1 kV had to be applied to achieve a modulation depth of nearly 50% at resonance (cf. Figure 12c). Modulation speeds of 100 kHz could be reached, though the high modulation depth was only observed in a rather small frequency range from 0.8 to 0.9 THz. In 2013, the same group investigated optical pumping of a similar structure at 800 nm.^[113] At a pump fluence of 18.7 $\mu\text{J cm}^{-2}$, a modulation depth of above 10% was reached. A sketch of the experiment is depicted in Figure 12d, the change in transmission as a function of the time delay between pump pulse and THz pulse is plotted in Figure 12e. As the lifetime of the photoexcited carriers in graphene is very small, the change in THz transmission persists only for about 5 ps, enabling ultrafast switching of THz radiation. Besides the change in THz transmission, a significant phase shift was observed, which will be discussed in more detail in Section 3.3.1.

The same group reported in 2013 a nonresonant graphene-metamaterial modulator.^[114] Instead of rings, square patches

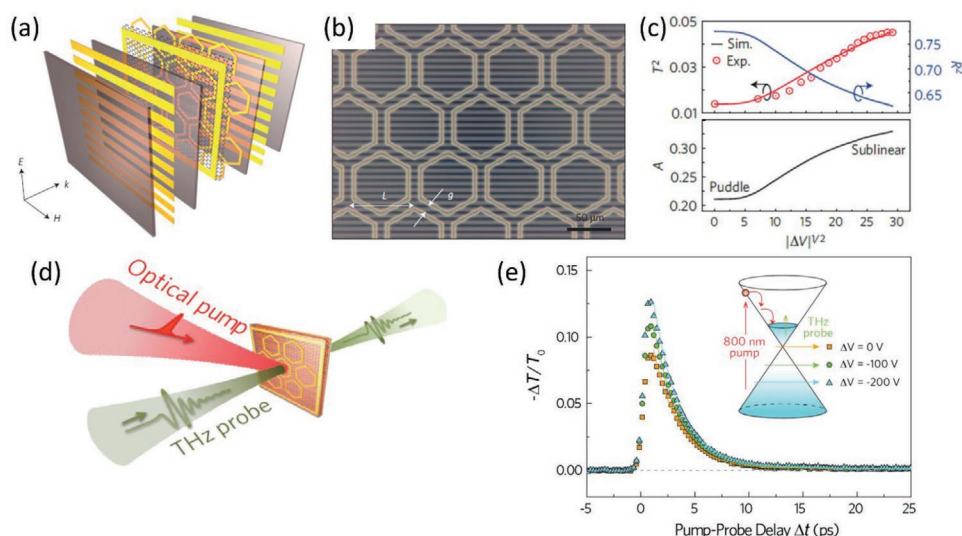


Figure 12. a) Sketch and b) microscope image of a hybrid graphene metamaterial modulator. c) Transmission and reflection through the sample as a function of the square root of the applied gate voltage measured at resonance. a–c) Reproduced with permission.^[112] Copyright 2012, Springer Nature. d) Schema of a NIR-pump THz-probe experiment to investigate optical pumping of a sample similar to the one depicted in (b). e) Pump-induced change in THz transmission as function of the pump–probe time delay. d,e) Reproduced with permission.^[113] Copyright 2013, Springer Nature.

with a size of about 10 μm are patterned with gaps on the μm range. Though a significant part of the surface is covered by gold, the transmission through the sample still reaches about 80%, showing no evident resonance in the range of 0.3–2.5 THz. Yet they report a broadband modulation depth of nearly 50%, comparable to the result of the resonant structure. Shi et al. followed a similar approach in 2015: they patterned gold stripes with small gaps that were covered with graphene, reaching a modulation depth of about 80%.^[115]

The concept of merging graphene with metallic metamaterial structures quickly spread in the THz community, leading to a variety of theoretical and experimental implementations. In 2012, Yan et al. presented theoretical results of a metal film with cross-shaped gaps in the vicinity of two graphene layers gating each other.^[116] While the resonance frequency remains nearly unchanged by gating, the proposed change in transmission can reach about 80% in a spectral width of about 20%.

One year later, Andryieuski et al. presented the concept of purely graphene-based metamaterials: patterned graphene in close proximity of a reflector can reach near 100% absorption, that can be quenched to below 20% by gating.^[36b] THz modulators based on metallic split-ring resonators (SRRs) on CVD grow graphene were demonstrated by Valmorra et al. and Degl'Innocenti et al., reaching modulation depth of 11.5%^[117] and 18%,^[118] respectively. In such devices, tuning the graphene conductivity mostly changes the quality factor of the SRR rather than manipulating the resonance frequency. Though the reported modulation depth is not superior to previously published results, the applied bias voltage in the 10^[117] and 1 V range^[118] are low enough for many real-world applications.

A different concept was introduced by Zhang et al. in 2014: cross-shaped gold elements are combined/connected by graphene stripes. In this case, the graphene serves as tunable inductors between the elements, which enables active control of the resonance frequency.^[119] The theoretical model of this structure predicts a tuning range of about 15% of the initial resonance frequency. An even larger tuning range in resonance frequency was published by Yang et al. in 2014. Rings with small, graphene filled gaps allowed a shift of the resonance frequency of about 40%.^[120] In contrast to prior studies, the focus was on minimizing the gated area, and consequently the parasitic capacitance. The gated area in such optimized devices covers only 0.032% of the device, potentially allowing fast modulation.

As in the case for unpatterned/plain large-area 2D materials discussed in Section 3.1, other 2D materials can also serve as active material in hybrid metamaterial THz modulators. Compared to graphene, the carrier mobility is rather low in most cases, e.g., TMDCs. On the other side, the bandgap permits the accumulation of optically excited electrons in the conduction band. As the optical absorption in these cases can be rather strong, lower optical excitation densities are required to reach a high modulation depth. On the other hand, the long lifetime of the optically excited carriers leads in most cases to a rather slow response. Zheng et al. demonstrated in 2016 an optically pumped THz modulator based on MoS₂-Si heterostructure.^[121] In a first step, SSR structures were lithographically fabricated on the Si substrate. Subsequently, MoS₂ was directly grown on the sample via chemical vapor deposition. A modulation depth over 90% was reached when the sample was pumped with

continuous wave radiation at 800 nm with a power density of 4 W cm⁻². Srivastava et al. also combined MoS₂ with an array of SSRs.^[122] The MoS₂ was drop cast on top of the patterned SRRs, the absorption was modulated by excitation with a femtosecond laser at 800 nm. At a pump-fluence of about 250 $\mu\text{J cm}^{-2}$ the resonance of the SSRs was completely quenched, leading to a modulation depth of the transmitted radiation of about 15%. The drop-casted MoS₂ provides a short carrier lifetime of less than 100 ps, making this type of modulator suitable for high speed modulation. Gopalan et al. reported very recently all-optical modulation with WS₂ at similar speed, reaching a modulation depth of about 40% when pumped with about 125 $\mu\text{J cm}^{-2}$.^[123]

3.2.2. Plasmonics

Instead of combining 2D materials with a resonant metallic structure, it can be directly patterned to plasmonically enhance the light-matter interaction drastically.^[18,19,124] Graphene patterned into micrometer wide ribbons can support collective oscillations of charge carriers in the THz range. The plasmon frequency in such structures can be tailored by the ribbon width, and tuned electro-statically by changing the carrier density (cf. **Figure 13**). If the electric field of the THz radiation is polarized perpendicular to the ribbons, the increase in light matter interaction leads to an absorption of well above 10% at resonance, while only Drude absorption is observed when the electric field is oriented along the ribbons. Ju et al. fabricated an array of graphene ribbons with various width in the micrometer range, ribbons with a width of 4 μm featured a plasmon frequency of about 3 THz.^[19] The ribbons were gated with a ionic gel that allowed to vary the carrier density in the range of 3×10^{12} – 1.4×10^{13} cm⁻². With this change in carrier density a modulation depth of more than 10% was observed in the spectral range from 2.4 to 3.9 THz. With polarization along the ribbons a similar modulation depth was found, caused by the Drude absorption. While a shift in the plasmon frequency was observed in the first case, the spectrally broad absorption did not change the shape with gate voltage (cf. **Figure 13c**).

To avoid the strong anisotropy of graphene ribbons, graphene can also be patterned into more symmetric structures, e.g., discs.^[125] Yan et al. observed isotropic response from discs fabricated from up to five layers of graphene. The strongest extinction of above 80% was observed for discs with a diameter of 8.6 μm and a periodicity of 9 μm . In this regime, the plasmons of neighboring discs are coupled, leading to a slight redshift of the plasmon frequency. As for the ribbons, the resonance frequency can be tailored by the diameter of the discs, though the stack of five graphene layers makes electro-static gating difficult. Nevertheless, the presented structure could be promising for all optical modulators as will be discussed later in this section. An alternative approach to increase the absorption of graphene plasmons, preserving the option to use electro-static gating, is the combination of graphene plasmons with gaps in metal sheets. Unlike in the studies presented in Section 3.2.1, where broadband modulation was observed when the gaps in a metal film were filled by graphene,^[114,115] Jadidi et al. designed the gaps to enable plasmonic response in the graphene

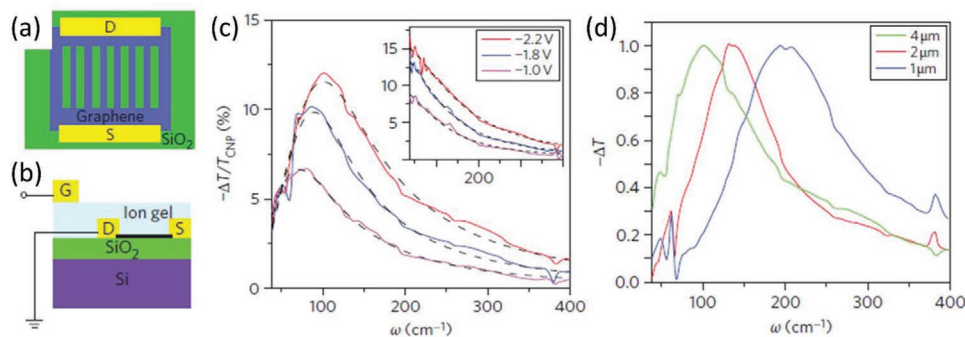


Figure 13. Top view a) and side view b) of the sample comprised of graphene microribbons on SiO₂/Si. c) Change of transmission through the sample at various gate voltages as a function of the inverse wavelength. At the resonance frequency of about 3 THz (100 cm⁻¹) the strongest change in transmission is observed. d) Extinction of ribbon arrays with various ribbon widths as a function of the inverse wavelength. Reproduced with permission.^[19] Copyright 2011, Springer Nature.

ribbons.^[126] A clear resonance was observed, gating lead to a modulation depth of about 60% of the transmitted radiation. Simulations in the same study suggest that a modulation depth of more than 80% might be possible by higher quality graphene with a mobility of 50 000 cm² V⁻¹ s⁻¹. This strong modulation in transmission is accompanied with a change of the plasmon frequency from about 2 to 6 THz, emphasizing the option to use such devices as tunable filters. A more complex structure was proposed by Zhao et al. in 2016: combining different resonant graphene elements, destructive interference leads to a pronounced plasmon-induced transparency.^[127] Again, electrostatic gating of the carrier density is expected to enable tuning of the plasmon frequency.

The strong linear absorption motivated theoreticians to investigate the plasmonic enhancement of nonlinear properties in patterned graphene. Gullans et al. predicted that even single photon switches based on graphene nanostructures should be feasible.^[128] The actual enhancement of the nonlinear absorption in an array of graphene ribbons in the THz range was first investigated by Jadidi et al.: performing degenerate pump-probe experiments with pump and probe polarization along the ribbons and perpendicular to the ribbons, the pump-induced change in transmission was found to be two orders of magnitude stronger when the plasmons were excited,^[54] though still only in the 1% range. As for unpatterned graphene, the carrier relaxation time was in the range of about 10 ps, enabling ultrafast modulation. Alongside the experimental results, a theoretical model based on hot carriers was presented. A more sophisticated theoretical model was presented by Cox et al. recently, confirming the important role of hot carriers.^[129]

Further experiments by Jadidi et al. shed more light on the role of the carrier mobility. While the sample presented in the initial study was based on CVD grown graphene with a carrier mobility of about 1000 cm² V⁻¹ s⁻¹, ribbons fabricated from quasi free-standing bilayer graphene with a mobility of ≈4000 cm² V⁻¹ s⁻¹ showed nearly a tenfold increase of the pump-induced change in transmission (cf. **Figure 14**) to about 10%. In addition to the measurements at resonance, tuning the photon frequency above and below the plasmon frequency lead to positive and negative changes in transmission, respectively (cf. **Figure 14d,e**). The negative signals below the resonance are actually caused by the thermal redshift of the plasmon frequency.

3.2.3. Waveguides

One major difficulty to achieve a strong light-matter interaction is the small interaction volume of the THz radiation with the 2D material. While resonant structures are a feasible way to enhance the absorption, this usually comes at the cost of a decreased modulation bandwidth. For the near-infrared range, guiding radiation along a 2D material was already demonstrated in 2011 by Liu et al.^[130] Khromova et al. proposed a variety of implementations of waveguide-integrated THz modulators in 2014.^[131] Combining several layers of graphene with a dielectric material in the center of a waveguide should lead to close to 100% modulation depth, even if the Fermi energy is changed in the meV range. Nevertheless, the realization of such a multilayer structure is difficult and has not been demonstrated so far. Xiao et al. presented in the following year a less complex concept, based on a graphene ribbon that is buried in polyethylene that guides the THz wave, a metal sheet in close proximity serves as gate electrode, efficiently changing the propagation length of the THz radiation. Modulation depth of above 70% were predicted when an optimized structure, consisting of three ribbons is fabricated.^[132] In the same year, Locatelli et al. presented their theoretical studies of a dielectric waveguide where graphene is deposited on the surface, i.e., only the evanescent field is propagating in the graphene layer.^[133] Two different cases are investigated: when the graphene is on top of the 70 μm wide and 2.5 mm long ridge, a modulation depth of up to 60% is proposed if two layers of graphene are employed. An increase of the evanescent field in the graphene layers is reached by introducing a 30 μm wide gap in the ridge, and depositing the graphene layers in the bottom of this gap. In this alternative approach, a modulation depth of about 80% is predicted, though the overall losses are higher. In both cases, the graphene covered area is rather small (2.5 × 0.07 and 2.5 × 0.03 mm²), making those structures promising for high speed modulation. Another theoretical study by Davoyan proposes a dielectric, cylindrical waveguide covered with graphene.^[134] The THz radiation is coupled to plasmons in the graphene sheet, allowing subwavelength dimensions of the waveguide. Though not discussed in detail in the manuscript, such a device could also function as a modulator, as the plasmons are only supported at high carrier density.

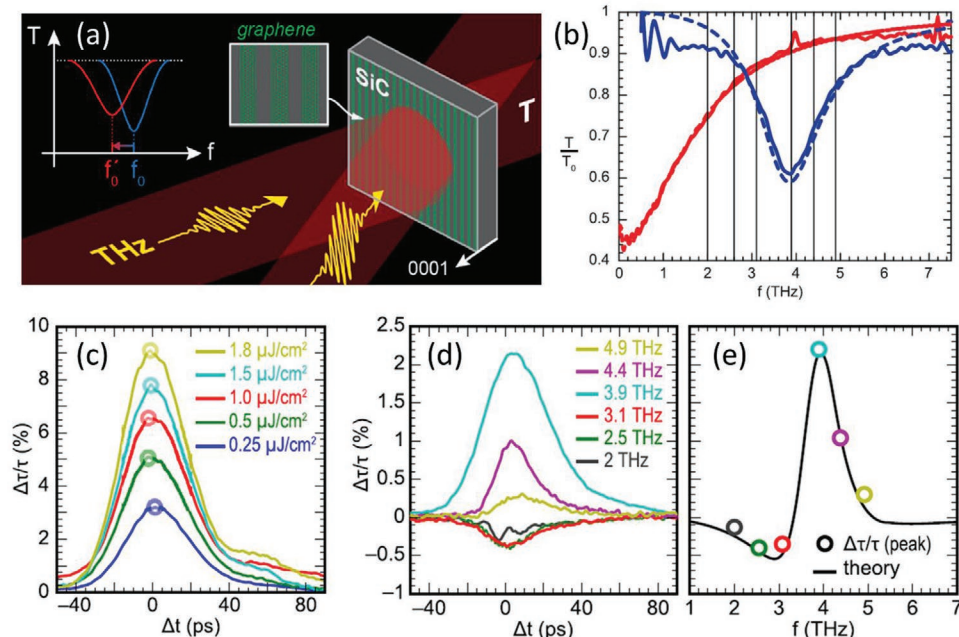


Figure 14. a) Sketch of the pump–probe experiment to investigate the nonlinear absorption in graphene ribbons. b) Transmission spectra of the unpatterned graphene (red line) and the graphene ribbons (blue line). The dashed lines represent Drude and Drude–Lorentz models. c) Pump-induced change in transmission as a function of the pump–probe delay measured at resonance (3.9 THz). d) Pump–probe signals measured at various frequencies at, above, and below resonance. e) Maximum change in transmission as a function of frequency. The circles represent the experimental results; the black line corresponds to a hot-carrier model. Adapted with permission.^[176] Copyright 2019, American Chemical Society.

In 2017, the first experimental realization of a graphene-based waveguide-integrated THz modulator was demonstrated.^[135] Two different designs were compared to each other: a simpler one with the graphene outside the waveguide, only penetrated by the evanescent field, and more complex one with the graphene sheet in the center of the waveguide (cf. Figure 15a–c). While for the simple device only for the lowest frequency components below 0.5 THz significant enhancement of modulation depth was observed (up to 50%), the design with the buried graphene sheet features a modulation depth of around 90% between 0.15 and 0.7 THz (cf. Figure 15d). While theoretical modeling of the waveguide predicts such modulation depth for a wide frequency range (to above 2 THz), the experimental modulation depth drops off steeply above 0.8 THz. The reason for this might be the excitation of higher order guided modes, leading to a lower efficiency in modulation.

Though not strictly being an independent THz modulator, we want to mention a device combining a graphene sheet with a THz quantum-cascade laser (QCL) here: by changing the conductivity of the graphene sheet that is in the vicinity of the top electrode, the output of the QCL can be completely quenched leading to a modulation depth of 100%. At the same time, the small electrode area enables fast modulation speed in the range of 100 MHz.^[136] The high modulation depth was speculated to be caused by THz absorption of the field inside the QCL resonator.

3.3. More Exotic Types of Modulators

So far we focused on intensity modulators, as those are the most common ones in the THz range. Beyond that, all other aspects of THz radiation can also be influenced. One recent

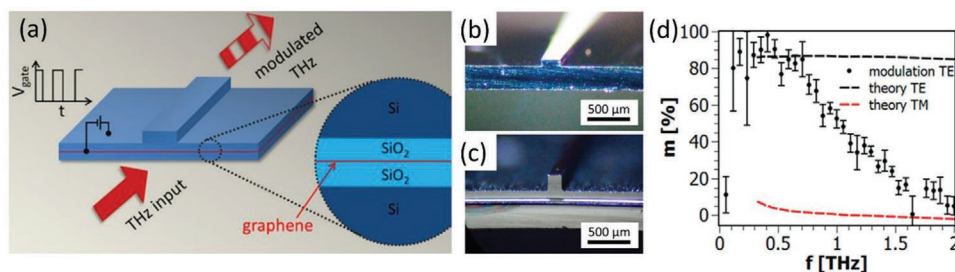


Figure 15. a) Sketch of the waveguide integrated THz modulator, the graphene sheet is implemented between two Si wafers. b, c) Optical micrograph of Si ridge waveguide with a graphene sheet on the bottom side (b) and in the center of the waveguide (c). d) Measured and modeled modulation depth of the waveguide shown in (c) as a function of frequency. Reproduced with permission.^[135] Copyright 2017, American Chemical Society.

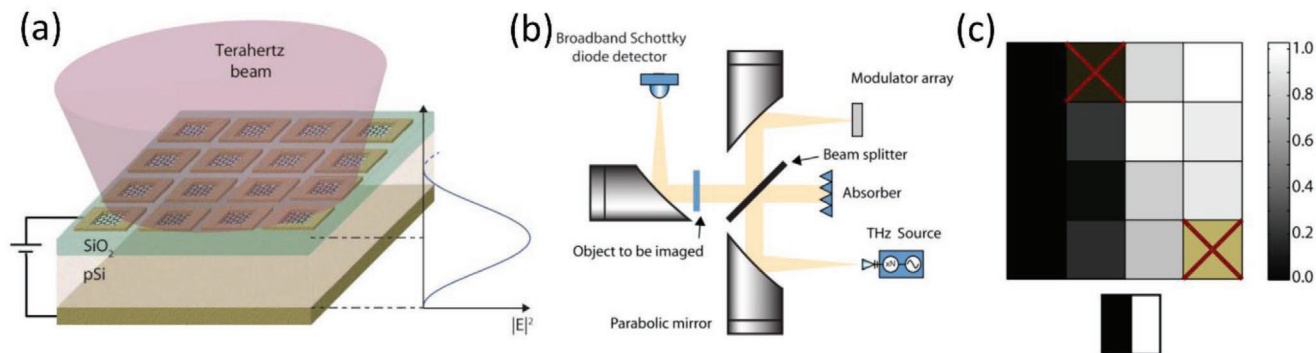


Figure 16. Sketch of a graphene-based reflective spatial light modulator a) and the test setup to pursue the imaging experiment with a single pixel detector b). c) Result of the measurement when the object is covering the left half of the THz beam (the crossed pixels were without function). Adapted with permission.^[177] Copyright 2013, Optical Society of America.

example is the polarization modulation of the THz radiation of a quantum-cascade laser: a combination of metallic split-ring resonators with patches of graphene in the gaps enables the rotation of THz polarization by up to 20° .^[137] In this last section, we want to briefly discuss two additional types of modulators, namely phase modulators and spatial modulators.

3.3.1. Phase Modulators

As wireless communication reaches out to the THz range, phase modulation can be included in the NIR part of THz generation via photoconductive emitters.^[138] Nevertheless, phase modulators that work independently of the THz source would be beneficial if other sources, e.g., QCLs are used. Modulators that are based on Drude absorption and allow high modulation depths have only minor effect on the phase of the transmitted THz radiation. For example, the waveguide integrated modulator achieved at 0.7 THz a modulation depth of about 90%, but the phase was modified by only 4° .^[135]

The situation is more promising for modulators based on resonant structures: even though the thickness of the active layer is far below the wavelengths, Lee et al. observed a gate-tunable change in phase of 32° .^[112] This phase change is attributed to the slight detuning of the resonance frequency of the metamaterial as the carrier density in the graphene sheet is varied by electro-static gating. Miao et al. presented in 2015 an optimized structure, based on the THz reflection of metallic resonant elements in close proximity of a graphene layer.^[139] In this case, the carrier density in the graphene sheet modifies the coupling between the elements, and thus the resonance frequency. Phase modulation of up to $\pm 180^\circ$ has been observed experimentally, demonstrating a potential device for real-world applications in the area of THz photonics.

3.3.2. Spatial Modulator

Spatial light modulation in the THz range paves the way for single pixel imaging^[80] or holographic displays.^[81] Sensale-Rodriguez et al. presented a reflective spatial light modulator with 4×4 pixels and demonstrated imaging with a single pixel

detector.^[82] Each pixel is composed of an active graphene area of $0.7 \times 0.7 \text{ mm}^2$ and can be independently electrically addressed. A SiO_2 layer on p-doped Si served as gate dielectric, a common back electrode was employed for gating as well as THz reflector, a sketch of the device is shown in Figure 16a. When the modulator is placed in the THz focus, the reflected and recollimated beam can be scanned over an object (cf. Figure 16b). As proof of principle, a scan of an object blocking the left half of the beam is shown in Figure 16c.

Kakenov et al. presented a spatial THz modulator that worked in transmission in 2015.^[140] In this case, horizontal and vertical graphene stripes that are separated by the gate dielectric, form a 5×5 array. A modulation depth of about 50% was reached for each pixel when the gate voltage was tuned by 2 V. While these two studies rely on fabrication of an array of independent graphene devices, large area modulators are expected to allow spatial light modulation with all above discussed all optical devices:^[141] exploiting a NIR or visible control beam (subwavelength) patterns can be projected on the large area device to spatially modify the THz properties,^[142] enabling ultra-fast devices with high resolution.

4. THz Emission

While the absorption or modulation of terahertz radiation has been extensively explored in a variety of 2D materials, the emission of THz radiation has received considerably less attention. Compared with other regions of the electromagnetic spectrum, efficient, bright, coherent terahertz optical sources are notoriously scarce. The search for new materials and optoelectronic methods for THz emission is therefore a compelling problem.

4.1. Pulsed THz Emission

When a material is excited by an optical pulse, it can produce a short transient photocurrent or induced polarization that can in both cases generate a propagating electromagnetic pulse. If the stimulus is sufficiently short in time (as, for example, that produced by a femtosecond laser), the resulting baseband electromagnetic pulse will have frequency components that extend

well into the terahertz regime.^[143] In bulk materials, an optically generated photocurrent is only produced in the presence of a DC bias field, and a rectified dielectric polarization only occurs in nonlinear materials that lack inversion symmetry. However, these constraints are relaxed or broken at surfaces and in 2D materials, when illuminated at non-normal incidence. Although 2D materials have not replaced traditional photoconductive semiconductors or nonlinear crystals as fast, efficient THz pulse sources, there have been numerous successful demonstrations of THz pulse generation in 2D materials, and the study of THz emission from 2D surfaces has shed light on the physics and carrier dynamics in these materials.

The earliest demonstration of pulsed THz emission from 2D materials was in graphite—the predecessor of graphene. Picosecond terahertz pulses are observed when graphite is illuminated off-axis by femtosecond near infrared pulses.^[144] The measurements showed no dependence on the crystallographic orientation of the graphite, and the polarization of the resulting THz transient indicates that the THz signal originates from an out-of-plane transient photocurrent—an effect that would be absent in truly 2D systems. The polarity of the THz wave was found to depend on doping of the graphite, which indicates the acceleration of carriers through space-charge effect or surface field in the graphite. Near-field THz probing further revealed that the response can be altered in geometrically patterned graphite elements.^[145]

Prechtel et al. observed picosecond photocurrents from suspended graphene in a coplanar stripline. The transient photocurrent was optically sampled using photoconductive detection in low-temperature-grown GaAs at the end of the stripline. The transient photocurrent was observed only when illuminated near the graphene-metal contact, and the origin was thought to be the hot-carrier photothermoelectric effect.^[146]

The photon drag effect can occur when graphene is illuminated off axis, in which case the in-plane momentum of the absorbed electron can produce a momentum mismatch between the generated electron and hole. As illustrated in **Figure 17**, this momentum shift upon off-axis illumination can be visualized by displacing the upper and lower Dirac cones by an amount that corresponds to the in-plane photon momentum. This displacement creates a net imbalance in the

carrier momentum that generates a measurable photocurrent. If the optical photon energy is close to the Pauli edge, the optical absorption can occur preferentially on one side of the Fermi cone,^[147] leading to a more significant photocurrent. This effect was observed and experimentally confirmed in monolayer graphene by characterizing the dependence of the THz polarization on the sample orientation and input optical polarization.^[148] The photon drag effect has also been observed at photon energies significantly above the Pauli edge, in which case the asymmetry between the conduction and valence bands plays a significant role,^[149] as illustrated in Figure 17. Bahk et al. showed that the THz emission from the photon drag effect can be significantly enhanced when the graphene layer is placed atop a metallic film, and back-illuminated through a prism, thereby exciting a propagating surface plasmon mode at the gold-graphene interface.^[150]

When graphene is illuminated at normal incidence, in most cases the symmetry of the illumination and material prohibit the generation of a THz transient. One notable exception is when the sample is coilluminated by phase-coherent, copolarized pulses at ω and 2ω . In this case, the coherent superposition of the two pulses can produce a net photocurrent with a direction that depends on the relative phase between the signal and its second-harmonic, especially if linear absorption of the lower-frequency fundamental pulse is inhibited by Pauli blocking. Sun et al. used this method to produce transient THz photocurrents in multilayer epitaxial graphene pumped at 3.2 and 1.6 μm .^[151]

Although graphene is the most extensively studied THz emitter, there have been several recent reports of THz pulse emission from semiconducting transition-metal dichalcogenides.^[152] Bulk layered WS_2 and WSe_2 exhibit a THz transient upon off-axis optical illumination, which is thought to be caused by acceleration of photogenerated carriers by a surface depletion field.^[153] However, polarization-resolved measurements of the THz transients produced in bulk layered MoS_2 point to an additional contribution from surface optical rectification.^[154] Recent studies of THz generation in monolayer WS_2 exhibit a distinctly different polarization- and angle-dependence, because in monolayer form, the vertical transient current is absent and the nonlinear response is thought to arise entirely from in-plane carrier dynamics and the lack of inversion symmetry.

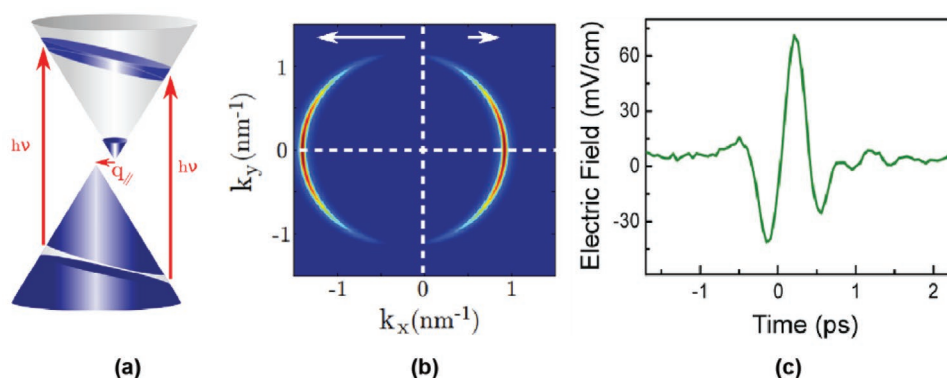


Figure 17. When graphene is illuminated by an off-axis optical pulse, the in-plane component of the photon momentum, denoted q_{\parallel} in (a), produces an asymmetry in the transient electron population, as illustrated in (b). The resulting transient photocurrent produces a picosecond THz pulse, shown in (c). Adapted with permission.^[149] Copyright 2014, American Chemical Society.

While 2D materials do not typically produce a terahertz transient pulse that is as strong or as that obtainable from traditional nonlinear or photoconductive materials, the emitted THz waveform and spectrum from 2D can hold information about the physical and dynamical processes in these materials. For example, transient THz emission spectroscopy was employed to observe ultrafast the interlayer charge transfer in 2D heterostructures of WS₂ and MoS₂.^[155]

4.2. Thermal THz Emission

Any hot object will emit a broad blackbody spectrum of radiation, characterized by the Planck spectral function

$$B(f, T) = \frac{2hf^3}{c^2} \frac{1}{\exp\left(\frac{hf}{k_B T}\right) - 1} \quad (10)$$

where f is the frequency, T is the temperature and B represents the spectral radiance of emitted light. For an object at room temperature, (9) predicts that the blackbody spectrum will have a maximum emission at 30 THz, but can include a continuum of lower frequencies spanning the lower-frequency THz regime. For hotter objects, the peak emission frequency shifts toward shorter wavelengths, but because the total emitted power scales as T^4 , the spectral emission in the THz tail (far from the peak) can dramatically increase with temperature.

Many 2D materials exhibit unusual thermal properties that allow the carriers and phonons to sustain a much higher temperature than the substrate when excited optically or electrically. Under these conditions, the 2D material can strongly emit thermal radiation. Unlike traditional thermal emitters, which are governed by slow cooling processes, THz emission by hot carriers in a 2D material can in principle be electrically modulated at high speed. Freitag et al., reported the first observation of thermal emission from graphene, in which the carriers were excited using Joule heating through an applied DC current.^[156] While their observations did not extend to the far infrared (THz), the measurements of the intensity of the infrared tail were consistent with Raman spectroscopy measurements, which showed a temperature of hundreds of degrees K. Lui et al. used optical illumination of graphene with femtosecond pulses to study the temporal behavior of

thermal emission. Under these conditions, measurements in the visible and near-infrared revealed an effective emission temperature of 2000–3200 K.^[157] These measurements suggest that the emission results from a combination of hot carriers and optical phonons in the 2D layer, which equilibrate among themselves on a timescale of hundreds of femtoseconds, but relax to the substrate much more slowly. Similar hot-carrier temperatures were achieved in suspended graphene by Kim et al. using DC electrical excitation, which was shown to result in bright thermal emission in the visible spectral range.^[158] Encapsulation of graphene in hexagonal boron nitride has also been effectively employed to inhibit thermal conduction to the substrate, thereby enabling thermal emission in the visible to mid-IR spectral regime.^[158b,159] While graphene remains the most explored 2D thermal emitter, thermal emission has also been observed in free-standing MoS₂, which is electrically heated through a DC current.^[160]

The aforementioned measurements have shown visible to infrared thermal emission from 2D materials that are consistent with an elevated temperature confined to the 2D layer. Although seldom observed, one can extrapolate the emission tail into the THz regime, according to the Planck distribution. However in the THz range, the wavelength can exceed the size of the 2D element, which further decreases the emitted terahertz power. Tong et al. employed a micrometer-scale graphene element connected to antenna, with a predicted resonant frequency of 1 THz. When the graphene was electrically heated by a DC electrical current, it was observed to emit a terahertz signal with spectral shape that resembled that of the antenna, attributed to thermal emission from the graphene.^[161] Li et al. have reported thermal emission from micrometer-scale graphene ribbons heated by a DC current, as shown in **Figure 18**, which exhibit a TM-polarized plasmon resonance in the terahertz regime that depends on the carrier concentration and ribbon size.^[162]

4.3. Stimulated Emission and Population Inversion

One of the most intriguing and compelling prospects for emission is through the stimulated emission of low-energy THz photons. Most direct bandgap semiconductors (both 2D and bulk) have a bandgap far above the THz regime, making them ill-suited for THz emission. Graphene's unique gapless

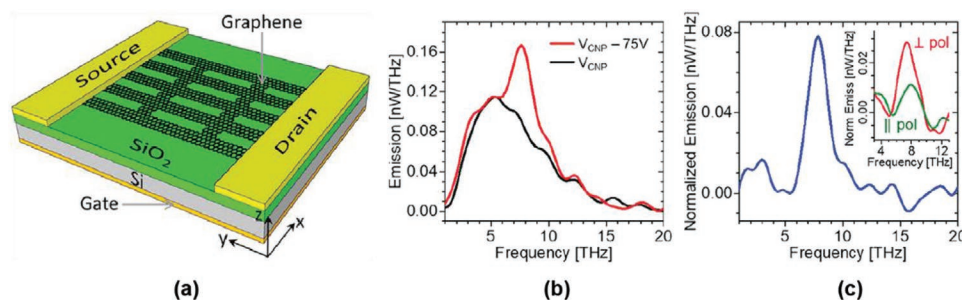


Figure 18. a) Graphene microribbons are electrically heated by a DC current, producing hot electrons. b) Measured terahertz emission spectrum for doped and charge-neutral graphene, showing enhanced thermal emission at the plasmon resonance frequency of the ribbons. c) Plasmonic component of the thermal emission, and polarization dependence. Adapted with permission.^[162] Copyright 2019, American Chemical Society.

dispersion relation makes it an interesting candidate for direct emission of low-energy THz photons, although there remains uncertainty whether it can support and sustain the requisite population inversion between electrons and holes.

The occupancy of energy levels in graphene in thermal equilibrium is described by the Fermi–Dirac distribution function described in Equation (9). This distribution, together with the dispersion relation and density of states, can explain all the salient linear absorption features of graphene, including direct frequency-independent interband absorption for photon energies $h\nu > 2E_F$, and intraband Drude absorption at THz frequencies. Critically, this distribution cannot yield conditions for stimulated emission, and the optical conductivity predicted by such a thermal distribution has a uniformly positive real part at all frequencies, associated with absorption and loss.

When graphene is optically or electrically excited, the carriers can achieve a nonequilibrium energy distribution. In most cases, the carriers are assumed to rapidly redistribute energy among themselves via electron–electron scattering, arriving at a new distribution that is still described by Equation (9), but with an electron temperature that exceeds that of the lattice. After the excitation or pumping ceases, the carrier temperature relaxes to the lattice temperature both through optical and acoustical phonon collisions that are heavily mediated by disorder and defects in the graphene. This two-temperature model of hot carriers in graphene has been used to explain a variety of optical and terahertz pump–probe observations. The relevant assumption of this model is that both electrons and holes are governed by the same Fermi distribution function, with a single temperature and chemical potential that applies across both the valence and conduction bands. Hence, the two-temperature hot-carrier description alone does not produce the conditions for negative conductivity or THz gain, but there remains debate over whether the carriers can achieve an inverted population during or prior to hot-carrier equilibration.

In 2007, Ryzhii et al. proposed a mechanism to achieve gain and population inversion in graphene via optical pumping.^[163] In this theory, a population of energetic electrons and holes at energy $\pm h\nu_0/2$ is initially produced by direct optical absorption of pump photons with frequency ν_0 , and they rapidly lose energy through cascaded emission of lower-energy optical phonons. Because the optical phonon energy for graphene is in the THz regime, the complete relaxation of carriers is inhibited below energies of a few THz, which is thought to produce an inverted accumulation of electrons and holes. This assumes, at least during the optical phonon emission process, that there are no competing relaxation mechanisms that would lead to further equilibration of the carriers. A similar process was proposed for achieving population inversion with electrical pumping, in which holes and electrons are laterally injected into an intrinsic graphene region through neighboring p- and n-type regions.^[164] In both pumping scenarios, the accumulation of electrons and holes after optical phonon relaxation is theoretically modeled with separate quasi-Fermi levels in the conduction and valence bands, describing the population of electrons and holes, respectively. When this assumption is used in place of (9), it leads to a dramatically different prediction for the optical conductivity. The intraband Drude absorption continues to produce free-carrier absorption, but if the populations

are inverted, the interband contribution is predicted to yield a conductivity with negative real portion, as a result of stimulated emission. When the negative conductivity from interband stimulated emission counterbalances the positive contribution from Drude absorption—conditions that are predicted to occur in the THz spectral regime under sufficient pumping—the graphene layer could theoretically exhibit THz gain and emission. The theory of population inversion was extended to the case of pulsed optical pumping in,^[165] using a model that allows for both heating and energy separation of carriers.

The degree of gain that could be achieved in single-pass transmission at normal incidence through graphene is theoretically limited to a few percent by the same mechanism that limits the interband absorption of photons above the Pauli edge. This problem could potentially be circumvented by employing multilayer graphene in vertical resonant cavities or dielectric waveguide structures.^[166] The gain could also be dramatically increased in traveling surface-plasmon modes. In this case, the slow group velocity of the plasmon mode and highly localized surface electromagnetic field have been predicted to yield a significant net plasmon gain^[167]—again under the assumption of an inverted carrier population.

The experimental evidence for stimulated emission and negative conductivity in graphene has been indirect and limited to pulsed optical excitation. Breusing et al. reported ultrafast optical pump–probe measurements of graphite, and posited that the results are best described by assuming separate quasi-Fermi levels for electrons and holes, rather than a single unified hot-carrier distribution.^[168] Li et al. used NIR optical pump–probe measurements to study the pump-induced change in reflection experienced by a coincident NIR probe pulse. They observed a transient decrease in the reflectivity that, at sufficiently high pump power, exceeded the level predicted when the optical conductivity σ is zero.^[169] They interpreted this as a signature of negative dynamic conductivity and stimulated emission, although the absence of concomitant transmission measurements precluded the experimental verification of optical gain.

Bouanga-Tombet et al. used terahertz time-domain spectroscopy of optically pumped graphene in an electrooptic Fabry–Perot geometry.^[170] They observed that the THz Fabry–Perot echo pulse was stronger under optical illumination, and suggested THz stimulated emission as the cause. However, the level of enhancement greatly exceeded the quantum limited gain for single-pass transmission, which prompted a reinterpretation that accounts for surface plasmon coupling. Other mechanisms such as enhanced surface reflectivity from photo-generated carriers could also complicate the interpretation of the observation.

More recently, Yadav et al. have employed two electrically-contacted graphene layers, separated by a hexagonal boron nitride insulating barrier—a capacitive structure that permits a separate population of electrons and holes on the two adjacent graphene layers. In this structure, stimulated emission would require resonant interlayer tunneling through the insulating barrier. Experimental evidence to date shows weak, broadband THz thermal emission when the device is biased,^[171] but to date there has been no conclusive evidence of stimulated emission.

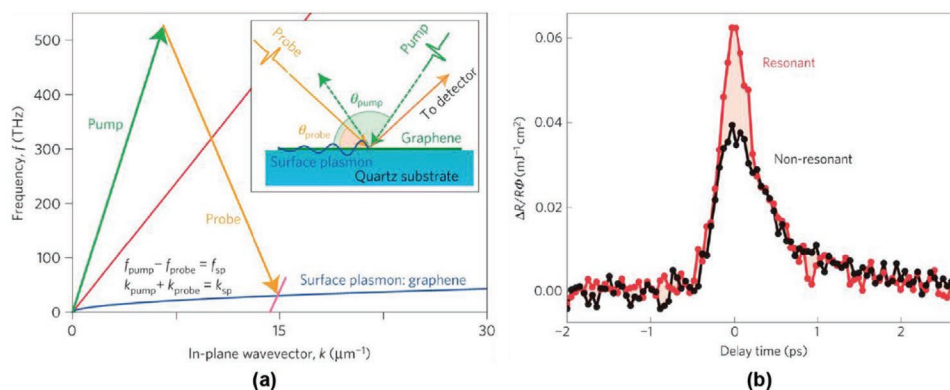


Figure 19. a) Phase-matching conditions for difference frequency mixing between NIR waves to produce a THz surface plasmon in a graphene monolayer. b) Increased reflection of the probe wave under resonant conditions provides indirect evidence of coupling to THz surface plasmon. Reproduced with permission.^[178] Copyright 2015, Springer Nature.

4.4. Difference Frequency Mixing

When two traveling waves overlap in space, they produce an interference pattern that oscillates at the difference frequency. In a second-order nonlinear material, the resulting interference pattern can in turn induce a nonlinear polarization that generates a third wave at the difference frequency. Difference frequency generation (DFG) in nonlinear crystals is often used to generate tunable mid-infrared waves and terahertz waves, but a critical requirement in these nonlinear optical crystals is phase-matching—the interference pattern must travel at a velocity that matches that of the terahertz wave to be generated.

2D materials are fundamentally different from traditional nonlinear crystals, in ways that might seem to make DFG impossible: a majority of 2D materials, including graphene, are centrosymmetric and therefore do not exhibit a second-order nonlinear effect, and moreover the 2D nature prohibits propagation of a traditional 3D electromagnetic wave. However, 2D conductive materials can support a traveling surface plasmon wave—a collective charge oscillation within the sheet that is connected to a localized electromagnetic wave that travels along the surface. In metals, these plasmon waves are typically observed at visible light frequencies, but in conductive 2D sheets, the motion happens at much slower terahertz frequencies, and the plasma frequency can be electrostatically tuned. The electromagnetic fields of the surface plasmon are confined to a subwavelength region in the vicinity of the surface, which could potentially enhance the nonlinear interaction. The wavelength of the plasmon wave is orders of magnitude smaller than the vacuum wavelength, which presents both challenges and opportunities for nonlinear phase matching.

Yao et al. considered the theory of THz difference frequency mixing between plane waves at a graphene interface, including the conditions for phase matching, and predicted a nonlinear susceptibility for DFG that is orders of magnitude higher than in traditional bulk materials.^[172] Shortly thereafter, Constant et al. reported an experimental measurement of this phenomena, by interfering two noncollinear femtosecond laser pulses at different wavelength. While they did not directly observe the resulting THz surface plasmon, the reflectivity of the longer wavelength “probe” pulse showed a marked decrease

when the phase matching conditions were met, indirectly providing evidence of a generated surface plasmon at 23.8 THz, as illustrated in **Figure 19**. They also highlight the importance of nonlocal effects in explaining the observed second-order nonlinearity. Others have more recently extended this method to continuous-wave difference frequency mixing between counter-propagating near-infrared signals in an optical waveguide. In this configuration, again the 7.5 THz surface plasmon was not directly observed, but the measurements show a marked decrease in the optical transmission when the phase matching condition was met.^[173] The theory of nonlinear difference frequency generation in graphene has been revisited in light of these experiments, and extended to include the effects of photon drag (momentum transfer from the photons to the electrons) and photothermal excitation.^[174]

5. Conclusion

The THz spectral regime is currently of scientific interest, but with the rapid advancement of consumer technologies in high-speed wireless communication, sensing, and navigation, we foresee an even greater need for submillimeter and THz devices and technologies in the near future. Optoelectronic devices that operate in the optical and near-infrared regime are now commonplace, but these technologies have not been translated to the THz regime, primarily because of shortcomings in the available materials. The remarkable tunable optical, electrical, and thermal properties of atomically thin materials make them well suited for current and future THz applications. This review highlights some of the recent developments and challenges in 2D THz optoelectronic technology, with an emphasis on devices for detecting, modulating and emitting THz radiation.

Among the panoply of available 2D materials, graphene stands out as the most mature and explored material for THz optoelectronics, and its unique gapless dispersion relation makes it especially applicable for THz applications. However, many of the newer semiconducting 2D materials have also recently shown a THz response, and even in thin materials that ultimately are ill-suited for practical THz optoelectronic devices,

THz measurements can provide unparalleled insight into the carrier and excitation dynamics. Complex heterostructures of stacked van der Waals materials offer even greater flexibility in the design and customization of 2D materials, that could bring greater functionality for future THz optoelectronics.

As highlighted here, research on 2D THz optoelectronics has already proved fruitful, and in many cases has yielded devices with performance that rivals or exceeds the state of the art. Despite this, the field is still in its early stages. Most of the results reported here are research demonstrations or proof-of-principle experiments, and have not yet found their way into commercial manufactured products or industrial applications. There is a need for greater reliability and repeatability in 2D device fabrication, as well as new methods for producing wafer-scale 2D materials with properties that match that of small exfoliated flakes. The promise of new high-performance THz devices could be a key factor that drives the development of new large-area material production.

Acknowledgements

Parts of the work by M.M. are funded by the Deutsche Forschungsgemeinschaft (DFG, German Research Foundation)—Project-ID 278162697—SFB 1242. Parts of the research of S.W. was funded by the Deutsche Forschungsgemeinschaft (DFG, German Research Foundation) via SPP 1459. Portions of this work by T.E.M. were supported by the Office of Naval Research (ONR; N000141310865) and the National Science Foundation (NSF) (ECCS 1309750).

Conflict of Interest

The authors declare no conflict of interest.

Keywords

far infrared, graphene, optoelectronics, terahertz, 2D materials

Received: August 31, 2020

Revised: October 21, 2020

Published online: December 9, 2020

- [1] a) C. Jansen, S. Wietzke, O. Peters, M. Scheller, N. Vieweg, M. Salhi, N. Krumbholz, C. Jördens, T. Hochrein, M. Koch, *Appl. Opt.* **2010**, 49, E48; b) D. M. Mittleman, M. Gupta, R. Neelamani, R. G. Baraniuk, J. V. Rudd, M. Koch, *Appl. Phys. B* **1999**, 68, 1085; c) K. Kawase, Y. Ogawa, Y. Watanabe, H. Inoue, *Opt. Express* **2003**, 11, 2549; d) H. Liu, H. Zhong, N. Karpowicz, Y. Chen, X. Zhang, *Proc. IEEE* **2007**, 95, 1514.
- [2] J. A. Zeitler, P. F. Taday, D. A. Newnham, M. Pepper, K. C. Gordon, T. Rades, *J. Pharm. Pharmacol.* **2007**, 59, 209.
- [3] a) Y. C. Shen, T. Lo, P. F. Taday, B. E. Cole, W. R. Tribe, M. C. Kemp, *Appl. Phys. Lett.* **2005**, 86, 241116; b) A. G. Davies, E. H. Linfield, M. Pepper, M. K. Choi, A. Bettermann, D. W. van der Weide, *Philos. Trans. R. Soc., A* **2004**, 362, 197.
- [4] a) P. H. Siegel, *IEEE Trans. Antennas Propag.* **2007**, 55, 2957; b) C. Kulesa, *IEEE Trans. THz Sci. Technol.* **2011**, 1, 232; c) V. Lattanzi, A. Walters, J. C. Pearson, B. J. Drouin, *J. Quant. Spectrosc. Radiat. Transfer* **2008**, 109, 580.
- [5] a) T. Kleine-Ostmann, T. Nagatsuma, *J. Infrared Millim. Terahertz Waves* **2011**, 32, 143; b) T. Nagatsuma, G. Ducournau, C. C. Renaud, *Nat. Photonics* **2016**, 10, 371.
- [6] a) Z. Lin, A. McCreary, N. Briggs, S. Subramanian, K. Zhang, Y. Sun, X. Li, N. J. Borys, H. Yuan, S. K. Fullerton-Shirey, A. Chernikov, H. Zhao, S. McDonnell, A. M. Lindenberg, K. Xiao, B. J. LeRoy, M. Drndić, J. C. M. Hwang, J. Park, M. Chhowalla, R. E. Schaak, A. Javey, M. C. Hersam, J. Robinson, M. Terrones, *2D Mater.* **2016**, 3, 042001; b) A. J. Mannix, B. Kiraly, M. C. Hersam, N. P. Guisinger, *Nat. Rev. Chem.* **2017**, 1, 0014; c) J. Shi, Z. Li, D. K. Sang, Y. Xiang, J. Li, S. Zhang, H. Zhang, *J. Mater. Chem. C* **2018**, 6, 1291.
- [7] D. De Fazio, D. G. Purdie, A. K. Ott, P. Braeuninger-Weimer, T. Khodkov, S. Goossens, T. Taniguchi, K. Watanabe, P. Livreri, F. H. L. Koppens, S. Hofmann, I. Goykman, A. C. Ferrari, A. Lombardo, *ACS Nano* **2019**, 13, 8926.
- [8] K. I. Bolotin, K. J. Sikes, Z. Jiang, M. Klima, G. Fudenberg, J. Hone, P. Kim, H. L. Stormer, *Solid State Commun.* **2008**, 146, 351.
- [9] Y. Akahama, S. Endo, S.-i. Narita, *J. Phys. Soc. Jpn.* **1983**, 52, 2148.
- [10] F. Xia, H. Wang, Y. Jia, *Nat. Commun.* **2014**, 5, 4458.
- [11] W. G. Cullen, M. Yamamoto, K. M. Burson, J. H. Chen, C. Jang, L. Li, M. S. Fuhrer, E. D. Williams, *Phys. Rev. Lett.* **2010**, 105, 215504.
- [12] M. Walther, D. G. Cooke, C. Sherstan, M. Hajar, M. R. Freeman, F. A. Hegmann, *Phys. Rev. B* **2007**, 76, 125408.
- [13] B. Sensale-Rodriguez, R. S. Yan, M. M. Kelly, T. Fang, K. Tahy, W. S. Hwang, D. Jena, L. Liu, H. G. Xing, *Nat. Commun.* **2012**, 3, 780.
- [14] a) X. Cai, A. B. Sushkov, R. J. Suess, M. M. Jadidi, G. S. Jenkins, L. O. Nyakiti, R. L. Myers-Ward, S. Li, J. Yan, D. K. Gaskill, T. E. Murphy, H. D. Drew, M. S. Fuhrer, *Nat. Nanotechnol.* **2014**, 9, 814; b) L. Viti, J. Hu, D. Coquillat, A. Politano, W. Knap, M. S. Vitiello, *Sci. Rep.* **2016**, 6, 20474.
- [15] R. R. Nair, P. Blake, A. N. Grigorenko, K. S. Novoselov, T. J. Booth, T. Stauber, N. M. R. Peres, A. K. Geim, *Science* **2008**, 320, 1308.
- [16] a) D. Jariwala, T. J. Marks, M. C. Hersam, *Nat. Mater.* **2016**, 16, 170; b) K. S. Novoselov, A. Mishchenko, A. Carvalho, A. H. Castro Neto, *Science* **2016**, 353, aac9439.
- [17] H. Yoon, K. Y. M. Yeung, P. Kim, D. Ham, *Philos. Trans. R. Soc., A* **2014**, 372, 20130104.
- [18] A. N. Grigorenko, M. Polini, K. S. Novoselov, *Nat. Photonics* **2012**, 6, 749.
- [19] L. Ju, B. S. Geng, J. Horng, C. Girit, M. Martin, Z. Hao, H. A. Bechtel, X. G. Liang, A. Zettl, Y. R. Shen, F. Wang, *Nat. Nanotechnol.* **2011**, 6, 630.
- [20] a) E. E. Haller, *Infrared Phys. Technol.* **1994**, 35, 127; b) Y.-S. Lee, *Principles of Terahertz Science and Technology*, Springer, New York **2009**; c) E. Bründermann, H.-W. Hübers, M. F. Kimmitt, *Terahertz Techniques*, Springer, Berlin **2012**.
- [21] A. D. Semenov, Y. P. Gousev, R. S. Nebosis, K. F. Renk, P. Yagoubov, B. M. Voronov, G. N. Gol'tsman, V. D. Syomash, E. M. Gershenzon, *Appl. Phys. Lett.* **1996**, 69, 260.
- [22] T. Otsuji, *IEEE Trans. THz Sci. Technol.* **2015**, 5, 1110.
- [23] a) A. W. Lee, Q. Hu, *Opt. Lett.* **2005**, 30, 2563; b) B. S. Karasik, A. V. Sergeev, D. E. Prober, *IEEE Trans. THz Sci. Technol.* **2011**, 1, 97.
- [24] F. Sizov, *Semicond. Sci. Technol.* **2018**, 33, 123001.
- [25] a) F. H. L. Koppens, T. Mueller, P. Avouris, A. C. Ferrari, M. S. Vitiello, M. Polini, *Nat. Nanotechnol.* **2014**, 9, 780; b) G. Wang, Y. Zhang, C. You, B. Liu, Y. Yang, H. Li, A. Cui, D. Liu, H. Yan, *Infrared Phys. Technol.* **2018**, 88, 149; c) C. Xie, C. Mak, X. Tao, F. Yan, *Adv. Funct. Mater.* **2017**, 27, 1603886.
- [26] A. Rogalski, *Adv. Opt. Photon.* **2019**, 11, 314.
- [27] A. Rogalski, M. Kopytko, P. Martyniuk, *Appl. Phys. Rev.* **2019**, 6, 021316.
- [28] Y. Wang, W. Wu, Z. Zhao, *Infrared Phys. Technol.* **2019**, 102, 103024.

- [29] a) C. Jiang, V. A. Shalygin, V. Y. Panevin, S. N. Danilov, M. M. Glazov, R. Yakimova, S. Lara-Avila, S. Kubatkin, S. D. Ganichev, *Phys. Rev. B* **2011**, *84*, 125429; b) J. Karch, C. Drexler, P. Olbrich, M. Fehrenbacher, M. Hirmer, M. M. Glazov, S. A. Tarasenko, E. L. Ivchenko, B. Birkner, J. Eroms, D. Weiss, R. Yakimova, S. Lara-Avila, S. Kubatkin, M. Ostler, T. Seyller, S. D. Ganichev, *Phys. Rev. Lett.* **2011**, *107*, 276601; c) J. Karch, P. Olbrich, M. Schmalzbauer, C. Zoth, C. Brinsteiner, M. Fehrenbacher, U. Würstbauer, M. M. Glazov, S. A. Tarasenko, E. L. Ivchenko, D. Weiss, J. Eroms, R. Yakimova, S. Lara-Avila, S. Kubatkin, S. D. Ganichev, *Phys. Rev. Lett.* **2010**, *105*, 227402; d) P. Olbrich, C. Drexler, L. E. Golub, S. N. Danilov, V. A. Shalygin, R. Yakimova, S. Lara-Avila, S. Kubatkin, B. Redlich, R. Huber, S. D. Ganichev, *Phys. Rev. B* **2013**, *88*, 245425.
- [30] a) B. S. Karasik, A. V. Sergeev, *IEEE Trans. Appl. Supercond.* **2005**, *15*, 618; b) A. Zoghi, H. R. Saghai, *Physica C* **2019**, *557*, 44.
- [31] C. B. McKitterick, H. Vora, X. Du, B. S. Karasik, D. E. Prober, *J. Low Temp. Phys.* **2014**, *176*, 291.
- [32] D. A. Bandurin, I. Gayduchenko, Y. Cao, M. Moskotin, A. Principi, I. V. Grigorieva, G. Goltsman, G. Fedorov, D. Svintsov, *Appl. Phys. Lett.* **2018**, *112*, 141101.
- [33] a) C. Liu, L. Wang, X. Chen, J. Zhou, W. Tang, W. Guo, J. Wang, W. Lu, *Nanoscale* **2018**, *10*, 5852; b) L. Viti, A. Politano, M. S. Vitiello, *APL Mater.* **2017**, *5*, 035602.
- [34] a) M. Mittendorff, S. Winnerl, J. Kamann, J. Eroms, D. Weiss, H. Schneider, M. Helm, *Appl. Phys. Lett.* **2013**, *103*, 021113; b) L. Vicarelli, M. S. Vitiello, D. Coquillat, A. Lombardo, A. C. Ferrari, W. Knap, M. Polini, V. Pellegrini, A. Tredicucci, *Nat. Mater.* **2012**, *11*, 865; c) A. Zak, M. A. Andersson, M. Bauer, J. Matukas, A. Lisauskas, H. G. Roskos, J. Stake, *Nano Lett.* **2014**, *14*, 5834.
- [35] R. Degl'Innocenti, L. Xiao, S. J. Kindness, V. S. Kamboj, B. Wei, P. Braeuninger-Weimer, K. Nakanishi, A. I. Aria, S. Hofmann, H. E. Beere, D. A. Ritchie, *J. Phys. D* **2017**, *50*, 174001.
- [36] a) J. Zhang, X. Wei, M. Premaratne, W. Zhu, *Photon. Res.* **2019**, *7*, 868; b) A. Andryieuski, A. V. Lavrinenko, *Opt. Express* **2013**, *21*, 9144; c) B.-z. Xu, C.-q. Gu, Z. Li, Z.-y. Niu, *Opt. Express* **2013**, *21*, 23803; d) X. Wang, X. Jiang, Q. You, J. Guo, X. Dai, Y. Xiang, *Photon. Res.* **2017**, *5*, 536.
- [37] S.-Y. Chiang, Y.-Y. Li, T.-L. Shen, M. Hofmann, Y.-F. Chen, *Nano Lett.* **2020**, *20*, 2326.
- [38] Z. Mics, K.-J. Tielrooij, K. Parvez, S. A. Jensen, I. Ivanov, X. Feng, K. Müllen, M. Bonn, D. Turchinovich, *Nat. Commun.* **2015**, *6*, 7655.
- [39] a) H. Y. Hwang, N. C. Brandt, H. Farhat, A. L. Hsu, J. Kong, K. A. Nelson, *J. Phys. Chem. B* **2013**, *117*, 15819; b) S. Winnerl, F. Göttfert, M. Mittendorff, H. Schneider, M. Helm, T. Winzer, E. Malic, A. Knorr, M. Orlita, M. Potemski, M. Sprinkle, C. Berger, W. A. de Heer, *J. Phys. Condens. Matter* **2013**, *25*, 054202; c) S. Winnerl, M. Orlita, P. Plochocka, P. Kossacki, M. Potemski, T. Winzer, E. Malic, A. Knorr, M. Sprinkle, C. Berger, W. A. de Heer, H. Schneider, M. Helm, *Phys. Rev. Lett.* **2011**, *107*, 237401.
- [40] M. Mittendorff, J. Kamann, J. Eroms, D. Weiss, C. Drexler, S. D. Ganichev, J. Kerbusch, A. Erbe, R. J. Suess, T. E. Murphy, S. Chatterjee, K. Kolata, J. Ohser, J. C. König-Otto, H. Schneider, M. Helm, S. Winnerl, *Opt. Express* **2015**, *23*, 28728.
- [41] S. Lara-Avila, A. Danilov, D. Golubev, H. He, K. H. Kim, R. Yakimova, F. Lombardi, T. Bauch, S. Cherednichenko, S. Kubatkin, *Nat. Astron.* **2019**, *3*, 983.
- [42] X. Liu, D. Wang, P. Wei, L. Zhu, J. Shi, *Phys. Rev. B* **2012**, *86*, 155414.
- [43] E. H. Hwang, E. Rossi, S. D. Sarma, *Phys. Rev. B* **2009**, *80*, 235415.
- [44] a) E. Leong, R. J. Suess, A. B. Sushkov, H. D. Drew, T. E. Murphy, M. Mittendorff, *Opt. Express* **2017**, *25*, 12666; b) L. Viti, A. Politano, K. Zhang, M. S. Vitiello, *Nanoscale* **2019**, *11*, 1995.
- [45] a) M. Dyakonov, M. Shur, *Phys. Rev. Lett.* **1993**, *71*, 2465; b) M. Dyakonov, M. Shur, *IEEE Trans. Electron Devices* **1996**, *43*, 380.
- [46] a) W. Knap, M. Dyakonov, D. Coquillat, F. Teppe, N. Dyakonova, J. Łusakowski, K. Karpierz, M. Sakowicz, G. Valušis, D. Seliuta, I. Kašalynas, A. El Fatimy, Y. M. Meziani, T. Otsuji, *J. Infrared Millim. Terahertz Waves* **2009**, *30*, 1319; b) W. Knap, H. Videliar, S. Nadar, D. Coquillat, N. Dyakonova, F. Teppe, M. Bialek, M. Grynberg, K. Karpierz, J. Lusakowski, K. Nogajewski, D. Seliuta, I. Kašalynas, G. Valušis, *Opto-Electron. Rev.* **2010**, *18*, 225.
- [47] D. Spirito, D. Coquillat, S. L. De Bonis, A. Lombardo, M. Bruna, A. C. Ferrari, V. Pellegrini, A. Tredicucci, W. Knap, M. S. Vitiello, *Appl. Phys. Lett.* **2014**, *104*, 061111.
- [48] a) R. M. G. K. P. Deshmukh, S. S. Prabhu, P. K. Basu, *AIP Adv.* **2018**, *8*, 125122; b) F. Bianco, D. Perenzoni, D. Convertino, S. L. De Bonis, D. Spirito, M. Perenzoni, C. Coletti, M. S. Vitiello, A. Tredicucci, *Appl. Phys. Lett.* **2015**, *107*, 131104.
- [49] X.-X. Yang, J.-D. Sun, H. Qin, L. Lv, L.-N. Su, B. Yan, X.-X. Li, Z.-P. Zhang, J.-Y. Fang, *Chin. Phys. B* **2015**, *24*, 047206.
- [50] L. Viti, J. Hu, D. Coquillat, W. Knap, A. Tredicucci, A. Politano, M. S. Vitiello, *Adv. Mater.* **2015**, *27*, 5567.
- [51] G. Fedorov, I. Gayduchenko, N. Titova, M. Moskotin, E. Obraztsova, M. Rybin, G. Goltsman, *Proc. SPIE* **2018**, *10680*, 1068007.
- [52] M. T. Schlecht, S. Preu, S. Malzer, H. B. Weber, *Sci. Rep.* **2019**, *9*, 11205.
- [53] D. A. Bandurin, D. Svintsov, I. Gayduchenko, S. G. Xu, A. Principi, M. Moskotin, I. Tretyakov, D. Yagodkin, S. Zhukov, T. Taniguchi, K. Watanabe, I. V. Grigorieva, M. Polini, G. N. Goltsman, A. K. Geim, G. Fedorov, *Nat. Commun.* **2018**, *9*, 5392.
- [54] M. M. Jadidi, J. C. König-Otto, S. Winnerl, A. B. Sushkov, H. D. Drew, T. E. Murphy, M. Mittendorff, *Nano Lett.* **2016**, *16*, 2734.
- [55] M. Freitag, T. Low, W. Zhu, H. Yan, F. Xia, P. Avouris, *Nat. Commun.* **2013**, *4*, 1951.
- [56] X. Cai, A. B. Sushkov, M. M. Jadidi, L. O. Nyakiti, R. L. Myers-Ward, D. K. Gaskill, T. E. Murphy, M. S. Fuhrer, H. D. Drew, *Nano Lett.* **2015**, *15*, 4295.
- [57] Y. Kawano, *Nanotechnology* **2013**, *24*, 214004.
- [58] J. Sonntag, A. Kurzmann, M. Geller, F. Queisser, A. Lorke, R. Schützhold, *New J. Phys.* **2017**, *19*, 063028.
- [59] a) T. Plötzing, T. Winzer, E. Malic, D. Neumaier, A. Knorr, H. Kurz, *Nano Lett.* **2014**, *14*, 5371; b) K. J. Tielrooij, J. C. W. Song, S. A. Jensen, A. Centeno, A. Pesquera, A. Zurutuza Elorza, M. Bonn, L. S. Levitov, F. H. L. Koppens, *Nat. Phys.* **2013**, *9*, 248; c) T. Winzer, A. Knorr, E. Malic, *Nano Lett.* **2010**, *10*, 4839.
- [60] a) M. Mittendorff, M. Orlita, M. Potemski, C. Berger, W. A. de Heer, H. Schneider, M. Helm, S. Winnerl, *New J. Phys.* **2014**, *16*, 123021; b) M. Mittendorff, F. Wendler, E. Malic, A. Knorr, M. Orlita, M. Potemski, C. Berger, W. A. de Heer, H. Schneider, M. Helm, S. Winnerl, *Nat. Phys.* **2014**, *11*, 75.
- [61] a) V. Ryzhii, V. Mitin, M. Ryzhii, N. Ryabova, T. Otsuji, *Appl. Phys. Express* **2008**, *1*, 063002; b) V. Ryzhii, M. Ryzhii, *Phys. Rev. B* **2009**, *79*, 245311; c) V. Ryzhii, M. Ryzhii, V. Mitin, T. Otsuji, *J. Appl. Phys.* **2010**, *107*, 054512.
- [62] X. Yang, A. Vorobiev, A. Generalov, M. A. Andersson, J. Stake, *Appl. Phys. Lett.* **2017**, *111*, 021102.
- [63] D. Suzuki, S. Oda, Y. Kawano, *Nat. Photonics* **2016**, *10*, 809.
- [64] a) A. El Fatimy, R. L. Myers-Ward, A. K. Boyd, K. M. Daniels, D. K. Gaskill, P. Barbara, *Nat. Nanotechnol.* **2016**, *11*, 335; b) A. El Fatimy, A. Nath, D. Kong Byoung, K. Boyd Anthony, L. Myers-Ward Rachael, M. Daniels Kevin, M. M. Jadidi, E. Murphy Thomas, D. K. Gaskill, P. Barbara, *Nanophotonics* **2018**, *7*, 735.
- [65] P. Seifert, X. Lu, P. Stepanov, J. R. Durán Retamal, J. N. Moore, K.-C. Fong, A. Principi, D. K. Efetov, *Nano Lett.* **2020**, *20*, 3459.
- [66] a) B. Knoll, F. Keilmann, *Opt. Commun.* **2000**, *182*, 321; b) N. Ocelic, A. Huber, R. Hillenbrand, *Appl. Phys. Lett.* **2006**, *89*, 101124.

- [67] F. Kuschewski, H. G. von Ribbeck, J. Döring, S. Winnerl, L. M. Eng, S. C. Kehr, *Appl. Phys. Lett.* **2016**, *108*, 113102.
- [68] a) J. Chen, M. Badioli, P. Alonso-González, S. Thongrattanasiri, F. Huth, J. Osmond, M. Spasenović, A. Centeno, A. Pesquera, P. Godignon, A. Zurutuza Elorza, N. Camara, F. J. G. de Abajo, R. Hillenbrand, F. H. L. Koppens, *Nature* **2012**, *487*, 77; b) Z. Fei, A. S. Rodin, G. O. Andreev, W. Bao, A. S. McLeod, M. Wagner, L. M. Zhang, Z. Zhao, M. Thiemens, G. Dominguez, M. M. Fogler, A. H. C. Neto, C. N. Lau, F. Keilmann, D. N. Basov, *Nature* **2012**, *487*, 82; c) M. Wagner, Z. Fei, A. S. McLeod, A. S. Rodin, W. Bao, E. G. Iwinski, Z. Zhao, M. Goldflam, M. Liu, G. Dominguez, M. Thiemens, M. M. Fogler, A. H. Castro Neto, C. N. Lau, S. Amarie, F. Keilmann, D. N. Basov, *Nano Lett.* **2014**, *14*, 894.
- [69] M. C. Giordano, S. Mastel, C. Liewald, L. L. Columbo, M. Brambilla, L. Viti, A. Politano, K. Zhang, L. Li, A. G. Davies, E. H. Linfield, R. Hillenbrand, F. Keilmann, G. Scamarcio, M. S. Vitiello, *Opt. Express* **2018**, *26*, 18423.
- [70] F. Mooshammer, F. Sandner, M. A. Huber, M. Zizlsperger, H. Weigand, M. Plankl, C. Weyrich, M. Lanus, J. Kampmeier, G. Mussler, D. Grützmacher, J. L. Boland, T. L. Cocker, R. Huber, *Nano Lett.* **2018**, *18*, 7515.
- [71] A. Woessner, P. Alonso-González, M. B. Lundeberg, Y. Gao, J. E. Barrios-Vargas, G. Navickaite, Q. Ma, D. Janner, K. Watanabe, A. W. Cummings, T. Taniguchi, V. Pruneri, S. Roche, P. Jarillo-Herrero, J. Hone, R. Hillenbrand, F. H. L. Koppens, *Nat. Commun.* **2016**, *7*, 10783.
- [72] M. B. Lundeberg, Y. Gao, A. Woessner, C. Tan, P. Alonso-González, K. Watanabe, T. Taniguchi, J. Hone, R. Hillenbrand, F. H. L. Koppens, *Nat. Mater.* **2016**, *16*, 204.
- [73] S. Mastel, M. B. Lundeberg, P. Alonso-González, Y. Gao, K. Watanabe, T. Taniguchi, J. Hone, F. H. L. Koppens, A. Y. Nikitin, R. Hillenbrand, *Nano Lett.* **2017**, *17*, 6526.
- [74] M. Tani, K. Sakai, H. Mimura, *Jpn. J. Appl. Phys.* **1997**, *36*, L1175.
- [75] a) E. Castro-Camus, L. Fu, J. Lloyd-Hughes, H. H. Tan, C. Jagadish, M. B. Johnston, *J. Appl. Phys.* **2008**, *104*, 053113; b) S. Winnerl, F. Peter, S. Nitsche, A. Dreyhaupt, B. Zimmermann, M. Wagner, H. Schneider, M. Helm, K. Kohler, *IEEE J. Sel. Top. Quantum* **2008**, *14*, 449.
- [76] N. Hunter, A. S. Mayorov, C. D. Wood, C. Russell, L. Li, E. H. Linfield, A. G. Davies, J. E. Cunningham, *Nano Lett.* **2015**, *15*, 1591.
- [77] P. A. Obraztsov, P. A. Chizhov, T. Kaplas, V. V. Bukin, M. Silvennoinen, C.-F. Hsieh, K. Konishi, N. Nemoto, M. Kuwata-Gonokami, *ACS Photonics* **2019**, *6*, 1780.
- [78] M. Mittendorff, R. J. Suess, E. Leong, T. E. Murphy, *Nano Lett.* **2017**, *17*, 5811.
- [79] M. Knorr, P. Steinleitner, J. Raab, I. Gronwald, P. Merkl, C. Lange, R. Huber, *Opt. Express* **2018**, *26*, 19059.
- [80] a) E. L. Wooten, K. M. Kissa, A. Yi-Yan, E. J. Murphy, D. A. Lafaw, P. F. Hallemeier, D. Maack, D. V. Attanasio, D. J. Fritz, G. J. McBrien, D. E. Bossi, *IEEE J. Sel. Top. Quantum* **2000**, *6*, 69; b) C. Wang, M. Zhang, X. Chen, M. Bertrand, A. Shams-Ansari, S. Chandrasekhar, P. Winzer, M. Loncar, *Nature* **2018**, *562*, 101.
- [81] P. Gopalan, B. Sensale-Rodriguez, *Adv. Opt. Mater.* **2020**, *8*, 1900550.
- [82] R. J. Suess, S. Winnerl, H. Schneider, M. Helm, C. Berger, W. A. de Heer, T. E. Murphy, M. Mittendorff, *ACS Photonics* **2016**, *3*, 1069.
- [83] S. Winnerl, F. Gottfert, M. Mittendorff, H. Schneider, M. Helm, T. Winzer, E. Malic, A. Knorr, M. Orlita, M. Potemski, M. Sprinkle, C. Berger, W. A. de Heer, *J. Phys.:Condens. Matter* **2013**, *25*, 054202.
- [84] H. A. Hafez, S. Kovalev, J. C. Deinert, Z. Mics, B. Green, N. Awari, M. Chen, S. Gernanskiy, U. Lehnert, J. Teichert, Z. Wang, K. J. Tielrooij, Z. Y. Liu, Z. P. Chen, A. Narita, K. Mullen, M. Bonn, M. Gensch, D. Turchinovich, *Nature* **2018**, *561*, 507.
- [85] J. H. Strait, H. N. Wang, S. Shivaraman, V. Shields, M. Spencer, F. Rana, *Nano Lett.* **2011**, *11*, 4902.
- [86] a) A. J. Frenzel, C. H. Lui, W. Fang, N. L. Nair, P. K. Herring, P. Jarillo-Herrero, J. Kong, N. Gedik, *Appl. Phys. Lett.* **2013**, *102*, 113111; b) H. A. Hafez, I. Al-Naib, M. M. Dignam, Y. Sekine, K. Oguri, F. Blanchard, D. G. Cooke, S. Tanaka, F. Komori, H. Hibino, T. Ozaki, *Phys. Rev. B* **2015**, *91*, 035422; c) J. N. Heyman, J. D. Stein, Z. S. Kaminski, A. R. Banman, A. M. Massari, J. T. Robinson, *J. Appl. Phys.* **2015**, *117*, 015101.
- [87] P. Weis, J. L. Garcia-Pomar, M. Hoh, B. Reinhard, A. Brodyanski, M. Rahm, *ACS Nano* **2012**, *6*, 9118.
- [88] Q. Li, Z. Tian, X. Q. Zhang, R. Singh, L. L. Du, J. Q. Gu, J. G. Han, W. L. Zhang, *Nat. Commun.* **2015**, *6*, 7082.
- [89] C. J. Docherty, P. Parkinson, H. J. Joyce, M. H. Chiu, C. H. Chen, M. Y. Lee, L. J. Li, L. M. Herz, M. B. Johnston, *ACS Nano* **2014**, *8*, 11147.
- [90] M. B. M. Krishna, J. Madeo, J. P. Urquizo, X. Zhu, S. Vinod, C. S. Tiwary, P. M. Ajayan, K. M. Dani, *Semicond. Sci. Technol.* **2018**, *33*, 084001.
- [91] C. He, L. P. Zhu, Q. Y. Zhao, Y. Y. Huang, Z. H. Yao, W. Y. Du, Y. H. He, S. J. Zhang, X. L. Xu, *Adv. Opt. Mater.* **2018**, *6*, 1800290.
- [92] Z. Fan, Z. Geng, W. Fang, X. Lv, Y. Su, S. Wang, J. Liu, H. Chen, *AIP Adv.* **2020**, *10*, 045304.
- [93] a) D. S. Yang, T. Jiang, X. A. Cheng, *Opt. Express* **2017**, *25*, 16364; b) Z. Y. Fan, Z. X. Geng, X. Q. Lv, Y. Su, Y. P. Yang, J. Liu, H. D. Chen, *Sci. Rep.* **2017**, *7*, 14828.
- [94] S. Chen, F. Fan, Y. P. Miao, X. T. He, K. L. Zhang, S. J. Chang, *Nanoscale* **2016**, *8*, 4713.
- [95] J. Qiao, S. Wang, Z. Wang, C. He, S. Zhao, X. Xiong, S. Wang, X. Zhang, X. Tao, *Adv. Opt. Mater.* **2020**, *8*, 2000160.
- [96] X. Liu, B. Zhang, G. C. Wang, W. Wang, H. Y. Ji, J. L. Shen, *Opt. Mater.* **2017**, *73*, 718.
- [97] J. Z. Zhou, T. Yang, D. Wang, Z. Wang, Z. Zhang, J. You, Z. Xu, X. Zheng, X. Cheng, *Photonic Sens.* **2019**, *9*, 268.
- [98] K. S. Novoselov, A. K. Geim, S. V. Morozov, D. Jiang, Y. Zhang, S. V. Dubonos, I. V. Grigorieva, A. A. Firsov, *Science* **2004**, *306*, 666.
- [99] B. Sensale-Rodriguez, T. Fang, R. S. Yan, M. M. Kelly, D. Jena, L. Liu, H. L. Xing, *Appl. Phys. Lett.* **2011**, *99*, 113104.
- [100] I. Maeng, S. Lim, S. J. Chae, Y. H. Lee, H. Choi, J. H. Son, *Nano Lett.* **2012**, *12*, 551.
- [101] Q. Mao, Q. Y. Wen, W. Tian, T. L. Wen, Z. Chen, Q. H. Yang, H. W. Zhang, *Opt. Lett.* **2014**, *39*, 5649.
- [102] B. Sensale-Rodriguez, R. S. Yan, S. Rafique, M. D. Zhu, W. Li, X. L. Liang, D. Gundlach, V. Protasenko, M. M. Kelly, D. Jena, L. Liu, H. G. Xing, *Nano Lett.* **2012**, *12*, 4518.
- [103] J. S. Gomez-Diaz, C. Moldovan, S. Capdevila, J. Romeu, L. S. Bernard, A. Magrez, A. M. Ionescu, J. Perruisseau-Carrier, *Nat. Commun.* **2015**, *6*, 6334.
- [104] Y. Wu, C. La-o-Vorakiat, X. P. Qiu, J. B. Liu, P. Deorani, K. Banerjee, J. Son, Y. F. Chen, E. E. M. Chia, H. Yang, *Adv. Mater.* **2015**, *27*, 1874.
- [105] J. B. Liu, P. J. Li, Y. F. Chen, X. B. Song, Q. Mao, Y. Wu, F. Qi, B. J. Zhang, J. R. He, H. S. Yang, Q. Y. Wen, W. L. Zhang, *Opt. Lett.* **2016**, *41*, 816.
- [106] O. Balci, E. O. Polat, N. Kakenov, C. Kocabas, *Nat. Commun.* **2015**, *6*, 6628.
- [107] Q. Sun, X. Chen, X. Liu, R. I. Stantchev, E. Pickwell-MacPherson, *Adv. Opt. Mater.* **2020**, *8*, 1900535.
- [108] a) R. L. Fante, M. T. McCormack, *IEEE Trans. Antennas Propag.* **1988**, *36*, 1443; b) J. M. Woo, M. S. Kim, H. W. Kim, J. H. Jang, *Appl. Phys. Lett.* **2014**, *104*, 081106.
- [109] A. C. Tasolamprou, A. D. Koulouklidis, C. Daskalaki, C. P. Mavidis, G. Kenanakis, G. Deligeorgis, Z. Viskadourakis, P. Kuzhir, S. Tzortzakakis, M. Kafesaki, E. N. Economou, C. M. Soukoulis, *ACS Photonics* **2019**, *6*, 720.

- [110] H. T. Chen, W. J. Padilla, J. M. O. Zide, A. C. Gossard, A. J. Taylor, R. D. Averitt, *Nature* **2006**, *444*, 597.
- [111] L. Wang, Y. X. Zhang, X. Q. Guo, T. Chen, H. J. Liang, X. L. Hao, X. Hou, W. Kou, Y. C. Zhao, T. C. Zhou, S. X. Liang, Z. Q. Yang, *Nanomaterials* **2019**, *9*, 965.
- [112] S. H. Lee, M. Choi, T. T. Kim, S. Lee, M. Liu, X. Yin, H. K. Choi, S. S. Lee, C. G. Choi, S. Y. Choi, X. Zhang, B. Min, *Nat. Mater.* **2012**, *11*, 936.
- [113] S. H. Lee, J. Choi, H. D. Kim, H. Choi, B. Min, *Sci. Rep.* **2013**, *3*, 2135.
- [114] S. H. Lee, H. D. Kim, H. J. Choi, B. Kang, Y. R. Cho, B. Min, *IEEE Trans. THz Sci. Technol.* **2013**, *3*, 764.
- [115] S. F. Shi, B. Zeng, H. L. Han, X. Hong, H. Z. Tsai, H. S. Jung, A. Zettl, M. F. Crommie, F. Wang, *Nano Lett.* **2015**, *15*, 372.
- [116] R. S. Yan, B. Sensale-Rodriguez, L. Liu, D. Jena, H. G. Xing, *Opt. Express* **2012**, *20*, 28664.
- [117] F. Valmorra, G. Scalari, C. Maissen, W. Y. Fu, C. Schonenberger, J. W. Choi, H. G. Park, M. Beck, J. Faist, *Nano Lett.* **2013**, *13*, 3193.
- [118] R. Degl'Innocenti, D. S. Jessop, Y. D. Shah, J. Sibik, J. A. Zeitler, P. R. Kidambi, S. Hofmann, H. E. Beere, D. A. Ritchie, *ACS Nano* **2014**, *8*, 2548.
- [119] Y. Zhang, Y. J. Feng, B. Zhu, J. M. Zhao, T. Jiang, *Opt. Express* **2014**, *22*, 22743.
- [120] K. Yang, S. C. Liu, S. Arezoomandan, A. Nahata, B. Sensale-Rodriguez, *Appl. Phys. Lett.* **2014**, *105*, 093105.
- [121] W. Zheng, F. Fan, M. Chen, S. Chen, S. J. Chang, *AIP Adv.* **2016**, *6*, 075105.
- [122] Y. K. Srivastava, A. Chaturvedi, M. Manjappa, A. Kumar, G. Dayal, C. Kloc, R. Singh, *Adv. Opt. Mater.* **2017**, *5*, 1700762.
- [123] P. Gopalan, A. Chanana, S. Krishnamoorthy, A. Nahata, M. A. Scarpulla, B. Sensale-Rodriguez, *Opt. Mater. Express* **2019**, *9*, 826.
- [124] a) F. H. L. Koppens, D. E. Chang, F. J. G. de Abajo, *Nano Lett.* **2011**, *11*, 3370; b) M. Jablan, H. Buljan, M. Soljacic, *Phys. Rev. B* **2009**, *80*, 245435; c) T. Low, P. Avouris, *ACS Nano* **2014**, *8*, 1086.
- [125] H. G. Yan, X. S. Li, B. Chandra, G. Tulevski, Y. Q. Wu, M. Freitag, W. J. Zhu, P. Avouris, F. N. Xia, *Nat. Nanotechnol.* **2012**, *7*, 330.
- [126] M. M. Jadidi, A. B. Sushkov, R. L. Myers-Ward, A. K. Boyd, K. M. Daniels, D. K. Gaskill, M. S. Fuhrer, H. D. Drew, T. E. Murphy, *Nano Lett.* **2015**, *15*, 7099.
- [127] X. L. Zhao, C. Yuan, L. Zhu, J. Q. Yao, *Nanoscale* **2016**, *8*, 15273.
- [128] M. Gullans, D. E. Chang, F. H. L. Koppens, F. J. G. de Abajo, M. D. Lukin, *Phys. Rev. Lett.* **2013**, *111*, 247401.
- [129] J. D. Cox, F. J. G. de Abajo, *Optica* **2018**, *5*, 429.
- [130] M. Liu, X. B. Yin, E. Ulin-Avila, B. S. Geng, T. Zentgraf, L. Ju, F. Wang, X. Zhang, *Nature* **2011**, *474*, 64.
- [131] I. Khromova, A. Andryieuski, A. Lavrinenko, *Laser Photonics Rev.* **2014**, *8*, 916.
- [132] B. G. Xiao, R. L. Sun, J. L. He, K. Qin, S. Kong, J. Chen, W. Xiumin, *IEEE Photonics Technol. Lett.* **2015**, *27*, 2190.
- [133] A. Locatelli, G. E. Town, C. De Angelis, *IEEE Trans. THz Sci. Technol.* **2015**, *5*, 351.
- [134] A. R. Davoyan, N. Engheta, *ACS Photonics* **2016**, *3*, 737.
- [135] M. Mittendorff, S. S. Li, T. E. Murphy, *ACS Photonics* **2017**, *4*, 316.
- [136] G. Z. Liang, X. N. Hu, X. C. Yu, Y. D. Shen, L. H. H. Li, A. G. Davies, E. H. Linfield, H. K. Liang, Y. Zhang, S. F. Yu, Q. J. Wang, *ACS Photonics* **2015**, *2*, 1559.
- [137] S. J. Kindness, N. W. Almond, W. Michailow, B. B. Wei, L. A. Jakob, K. Delfanazari, P. Braeuninger-Weimer, S. Hofmann, H. E. Beere, D. A. Ritchie, R. Degl'Innocenti, *ACS Photonics* **2019**, *6*, 1547.
- [138] X. Y. Li, J. J. Yu, K. H. Wang, M. Kong, W. Zhou, Z. H. Zhu, C. Wang, M. M. Zhao, G. K. Chang, *J. Lightwave Technol.* **2019**, *37*, 606.
- [139] Z. Q. Miao, Q. Wu, X. Li, Q. He, K. Ding, Z. H. An, Y. B. Zhang, L. Zhou, *Phys. Rev. X* **2015**, *5*, 041027.
- [140] N. Kakenov, T. Takan, V. A. Ozkan, O. Balci, E. O. Polat, H. Altan, C. Kocabas, *Opt. Lett.* **2015**, *40*, 1984.
- [141] Q. Y. Wen, W. Tian, Q. Mao, Z. Chen, W. W. Liu, Q. H. Yang, M. Sanderson, H. W. Zhang, *Sci. Rep.* **2014**, *4*, 7409.
- [142] Z. W. Xie, X. K. Wang, J. S. Ye, S. F. Feng, W. F. Sun, T. Akalin, Y. Zhang, *Sci. Rep.* **2013**, *3*, 3347.
- [143] a) A. Nahata, A. S. Weling, T. F. Heinz, *Appl. Phys. Lett.* **1996**, *69*, 2321; b) Y. C. Shen, P. C. Upadhyaya, E. H. Linfield, H. E. Beere, A. G. Davies, *Appl. Phys. Lett.* **2003**, *83*, 3117.
- [144] a) G. Ramakrishnan, R. Chakkittakandy, P. C. M. Planken, *Opt. Express* **2009**, *17*, 16092; b) M. Irfan, J.-H. Yim, C. Kim, S. Wook Lee, Y.-D. Jho, *Appl. Phys. Lett.* **2013**, *103*, 201108.
- [145] M. Nagel, A. Michalski, T. Botzem, H. Kurz, *Opt. Express* **2011**, *19*, 4667.
- [146] L. Prechtel, L. Song, D. Schuh, P. Ajayan, W. Wegscheider, A. W. Holleitner, *Nat. Commun.* **2012**, *3*, 646.
- [147] M. V. Entin, L. I. Magarill, D. L. Shepelyansky, *Phys. Rev. B* **2010**, *81*, 165441.
- [148] P. A. Obratsov, N. Kanda, K. Konishi, M. Kuwata-Gonokami, S. V. Garnov, A. N. Obratsov, Y. P. Svirko, *Phys. Rev. B* **2014**, *90*, 241416.
- [149] J. Maysonnave, S. Huppert, F. Wang, S. Maero, C. Berger, W. de Heer, T. B. Norris, L. A. De Vaultier, S. Dhillion, J. Tignon, R. Ferreira, J. Mangeney, *Nano Lett.* **2014**, *14*, 5797.
- [150] Y.-M. Bahk, G. Ramakrishnan, J. Choi, H. Song, G. Choi, Y. H. Kim, K. J. Ahn, D.-S. Kim, P. C. M. Planken, *ACS Nano* **2014**, *8*, 9089.
- [151] D. Sun, C. Divin, J. Rioux, J. E. Sipe, C. Berger, W. A. de Heer, P. N. First, T. B. Norris, *Nano Lett.* **2010**, *10*, 1293.
- [152] Y. Huang, Z. Yao, C. He, L. Zhu, L. Zhang, J. Bai, X. Xu, *J. Phys.: Condens. Matter* **2019**, *31*, 153001.
- [153] a) L. Zhang, Y. Huang, Q. Zhao, L. Zhu, Z. Yao, Y. Zhou, W. Du, X. Xu, *Phys. Rev. B* **2017**, *96*, 155202; b) K. Si, Y. Huang, Q. Zhao, L. Zhu, L. Zhang, Z. Yao, X. Xu, *Appl. Surf. Sci.* **2018**, *448*, 416.
- [154] a) Y. Huang, L. Zhu, Z. Yao, L. Zhang, C. He, Q. Zhao, J. Bai, X. Xu, *J. Phys. Chem. C* **2018**, *122*, 481; b) Y. Huang, L. Zhu, Q. Zhao, Y. Guo, Z. Ren, J. Bai, X. Xu, *ACS Appl. Mater. Interfaces* **2017**, *9*, 4956.
- [155] E. Y. Ma, B. Guzelturk, G. Li, L. Cao, Z.-X. Shen, A. M. Lindenberg, T. F. Heinz, *Sci. Adv.* **2019**, *5*, eaau0073.
- [156] M. Freitag, H.-Y. Chiu, M. Steiner, V. Perebeinos, P. Avouris, *Nat. Nanotechnol.* **2010**, *5*, 497.
- [157] C. H. Lui, K. F. Mak, J. Shan, T. F. Heinz, *Phys. Rev. Lett.* **2010**, *105*, 127404.
- [158] a) Y. D. Kim, H. Kim, Y. Cho, J. H. Ryoo, C.-H. Park, P. Kim, Y. S. Kim, S. Lee, Y. Li, S.-N. Park, Y. Shim Yoo, D. Yoon, V. E. Dorgan, E. Pop, T. F. Heinz, J. Hone, S.-H. Chun, H. Cheong, S. W. Lee, M.-H. Bae, Y. D. Park, *Nat. Nanotechnol.* **2015**, *10*, 676; b) Y. D. Kim, Y. Gao, R.-J. Shiue, L. Wang, O. B. Aslan, M.-H. Bae, H. Kim, D. Seo, H.-J. Choi, S. H. Kim, A. Nemilentsau, T. Low, C. Tan, D. K. Efetov, T. Taniguchi, K. Watanabe, K. L. Shepard, T. F. Heinz, D. Englund, J. Hone, *Nano Lett.* **2018**, *18*, 934.
- [159] a) H. R. Barnard, E. Zosimova, N. H. Mahlmeister, L. M. Lawton, I. J. Luxmoore, G. R. Nash, *Appl. Phys. Lett.* **2016**, *108*, 131110; b) S.-K. Son, M. Šiškins, C. Mullan, J. Yin, V. G. Kravets, A. Kozikov, S. Ozdemir, M. Alhazmi, M. Holwill, K. Watanabe, T. Taniguchi, D. Ghazaryan, K. S. Novoselov, V. I. Fal'ko, A. Mishchenko, *2D Mater.* **2017**, *5*, 011006.
- [160] L. Dobusch, S. Schuler, V. Perebeinos, T. Mueller, *Adv. Mater.* **2017**, *29*, 1701304.
- [161] J. Tong, M. Muthee, S.-Y. Chen, S. K. Yngvesson, J. Yan, *Nano Lett.* **2015**, *15*, 5295.
- [162] Y. Li, P. Ferreyra, A. K. Swan, R. Paiella, *ACS Photonics* **2019**, *6*, 2562.
- [163] V. Ryzhii, M. Ryzhii, T. Otsuji, *J. Appl. Phys.* **2007**, *101*, 083114.
- [164] a) M. Ryzhii, V. Ryzhii, *Jpn. J. Appl. Phys.* **2007**, *46*, L151; b) V. Ryzhii, M. Ryzhii, V. Mitin, T. Otsuji, *J. Appl. Phys.* **2011**, *110*, 094503.

- [165] A. Satou, V. Ryzhii, Y. Kurita, T. Otsuji, *J. Appl. Phys.* **2013**, *113*, 143108.
- [166] a) V. Ryzhii, A. A. Dubinov, T. Otsuji, V. Mitin, M. S. Shur, *J. Appl. Phys.* **2010**, *107*, 054505; b) V. Ryzhii, M. Ryzhii, A. Satou, T. Otsuji, A. A. Dubinov, V. Y. Aleshkin, *J. Appl. Phys.* **2009**, *106*, 084507.
- [167] a) V. V. Popov, O. V. Polischuk, A. R. Davoyan, V. Ryzhii, T. Otsuji, M. S. Shur, *Phys. Rev. B* **2012**, *86*, 195437; b) F. Rana, *IEEE Trans. Nanotechnol.* **2008**, *7*, 91; c) T. Watanabe, T. Fukushima, Y. Yabe, S. A. Boubanga Tombet, A. Satou, A. A. Dubinov, V. Y. Aleshkin, V. Mitin, V. Ryzhii, T. Otsuji, *New J. Phys.* **2013**, *15*, 075003; d) A. A. Dubinov, V. Y. Aleshkin, V. Mitin, T. Otsuji, V. Ryzhii, *J. Phys.: Condens. Matter* **2011**, *23*, 145302.
- [168] M. Breusing, C. Ropers, T. Elsaesser, *Phys. Rev. Lett.* **2009**, *102*, 086809.
- [169] T. Li, L. Luo, M. Hupalo, J. Zhang, M. C. Tringides, J. Schmalian, J. Wang, *Phys. Rev. Lett.* **2012**, *108*, 167401.
- [170] a) S. Boubanga-Tombet, S. Chan, T. Watanabe, A. Satou, V. Ryzhii, T. Otsuji, *Phys. Rev. B* **2012**, *85*, 035443; b) H. Karasawa, T. Komori, T. Watanabe, A. Satou, H. Fukidome, M. Suemitsu, V. Ryzhii, T. Otsuji, *J. Infrared Millim. Terahertz Waves* **2011**, *32*, 655.
- [171] D. Yadav, S. B. Tombet, T. Watanabe, S. Arnold, V. Ryzhii, T. Otsuji, *2D Mater.* **2016**, *3*, 045009.
- [172] X. Yao, M. Tokman, A. Belyanin, *Phys. Rev. Lett.* **2014**, *112*, 055501.
- [173] B. Yao, Y. Liu, S.-W. Huang, C. Choi, Z. Xie, J. F. Flores, Y. Wu, M. Yu, D.-L. Kwong, Y. Huang, Y. Rao, X. Duan, C. W. Wong, *Nat. Photonics* **2018**, *12*, 22.
- [174] a) H. Rostami, M. I. Katsnelson, M. Polini, *Phys. Rev. B* **2017**, *95*, 035416; b) C. J. Tollerton, J. Bohn, T. J. Constant, S. A. R. Horsley, D. E. Chang, E. Hendry, D. Z. Li, *Sci. Rep.* **2019**, *9*, 3267.
- [175] S. Winnerl, M. Mittendorff, J. C. König-Otto, H. Schneider, M. Helm, T. Winzer, A. Knorr, E. Malic, *Ann. Phys. (Berlin)* **2017**, *529*, 1700022.
- [176] M. M. Jadidi, K. M. Daniels, R. L. Myers-Ward, D. K. Gaskill, J. C. König-Otto, S. Winnerl, A. B. Sushkov, H. D. Drew, T. E. Murphy, M. Mittendorff, *ACS Photonics* **2019**, *6*, 302.
- [177] B. Sensale-Rodriguez, S. Rafique, R. S. Yan, M. D. Zhu, V. Protasenko, D. Jena, L. Liu, H. G. Xing, *Opt. Express* **2013**, *21*, 2324.
- [178] T. J. Constant, S. M. Hornett, D. E. Chang, E. Hendry, *Nat. Phys.* **2015**, *12*, 124.
- [179] H. Qin, J. Sun, S. Liang, X. Li, X. Yang, Z. He, C. Yu, Z. Feng, *Carbon* **2017**, *116*, 760.
- [180] A. A. Generalov, M. A. Andersson, X. Yang, A. Vorobiev, J. Stake, *IEEE Trans. THz Sci. Technol.* **2017**, *7*, 614.
- [181] R. Degl'Innocenti, L. Xiao, D. S. Jessop, S. J. Kindness, Y. Ren, H. Lin, J. A. Zeitler, J. A. Alexander-Webber, H. J. Joyce, P. Braeuninger-Weimer, S. Hofmann, H. E. Beere, D. A. Ritchie, *ACS Photonics* **2016**, *3*, 1747.
- [182] L. Wang, C. Liu, X. Chen, J. Zhou, W. Hu, X. Wang, J. Li, W. Tang, A. Yu, S.-W. Wang, W. Lu, *Adv. Funct. Mater.* **2017**, *27*, 1604414.
- [183] H. Liu, Z. Chen, X. Chen, S. Chu, J. Huang, R. Peng, *J. Mater. Chem. C* **2016**, *4*, 9399.
- [184] A. Poglitsch, C. Waelkens, N. Geis, H. Feuchtgruber, B. Vandebussche, L. Rodriguez, O. Krause, E. Renotte, C. van Hoof, P. Saraceno, J. Cepa, F. Kerschbaum, P. Agnès, B. Ali, B. Altieri, P. Andreani, J. L. Augueres, Z. Balog, L. Barl, O. H. Bauer, N. Belbachir, M. Benedettini, N. Billot, O. Boulade, H. Bischof, J. Blommaert, E. Callut, C. Cara, R. Cerulli, D. Cesarsky, A. Contursi, Y. Creten, W. De Meester, V. Doublier, E. Doumayrou, L. Duband, K. Exter, R. Genzel, J. M. Gillis, U. Grözinger, T. Henning, J. Herreros, R. Huygen, M. Inguscio, G. Jakob, C. Jamar, C. Jean, J. de Jong, R. Katterloher, C. Kiss, U. Klaas, D. Lemke, D. Lutz, S. Madden, B. Marquet, J. Martignac, A. Mazy, P. Merken, F. Montfort, L. Morbidelli, T. Müller, M. Nielbock, K. Okumura, R. Orfei, R. Ottensamer, S. Pezzuto, P. Popesso, J. Putzeys, S. Regibo, V. Reveret, P. Royer, M. Sauvage, J. Schreiber, J. Stegmaier, D. Schmitt, J. Schubert, E. Sturm, M. Thiel, G. Tofani, R. Vavrek, M. Wetzstein, E. Wieprecht, E. Wierorrek, *Astron. Astrophys.* **2010**, *518*, L2.
- [185] A. Rogalski, F. Sizov, *Opto-Electron. Rev.* **2011**, *19*, 346.
- [186] N. Oda, A. W. M. Lee, T. Ishi, I. Hosako, Q. Hu, *Proc. SPIE* **2012**, *8363*, 83630A.
- [187] F. Schuster, D. Coquillat, H. Videlier, M. Sakowicz, F. Teppe, L. Dussopt, B. Giffard, T. Skotnicki, W. Knap, *Opt. Express* **2011**, *19*, 7827.
- [188] Y. Kurita, G. Ducournau, D. Coquillat, A. Satou, K. Kobayashi, S. Boubanga Tombet, Y. M. Meziani, V. V. Popov, W. Knap, T. Suemitsu, T. Otsuji, *Appl. Phys. Lett.* **2014**, *104*, 251114.



Martin Mittendorff studied photonics and image processing at the University of Applied Sciences in Darmstadt, where he received his degree (Dipl. Ing. (FH)) in 2010. From 2010 to 2014, he worked on his Ph.D. studies on carrier dynamics in graphene at the Helmholtz-Zentrum Dresden-Rossendorf and received his Ph.D. in 2014 from the Technical University Dresden. He then joined the Institute for Research in Electronics and Applied Physics at the University of Maryland to investigate black phosphorus and graphene. In 2018, he joined the University of Duisburg-Essen, his current research is focusing on time-resolved THz spectroscopy on 2D materials.



Stephan Winnerl received the Diploma and Ph.D. degrees in physics from the University of Regensburg, Germany, in 1996 and 1999, respectively. He was with the Forschungszentrum Jülich as postdoctoral member from 1999 to 2002. Since 2002, he has been with the Helmholtz-Zentrum Dresden-Rossendorf (HZDR), Germany, and was appointed as HZDR Research Fellow in 2014. His research interests include ultrafast and nonlinear spectroscopy of semiconductor quantum structures and 2D materials, in particular in the THz frequency range. Furthermore, he develops emitters and fast detectors for THz radiation.



Thomas E. Murphy received B.S. degrees in Electrical Engineering and Physics from Rice University in 1994. He then studied Electrical and Computer Engineering at Massachusetts Institute of Technology, receiving the M.S. degree in 1997 and Ph.D. degree in 2001. He was employed as a member of the technical staff at MIT Lincoln Laboratory from 2001 to 2002, and joined the faculty at the University of Maryland in 2002. His research interests include terahertz and microwave photonics, 2D optoelectronics, integrated optics, nonlinear and ultrafast optics, electrooptics, and nonlinear dynamical systems.